ARTICLES
https://doi.org/10.1038/s41563-018-0206-2
nature materials

Molecular sieving of ethylene from ethane using a rigid metal–organic framework

Rui-Biao Lin[1,6], Libo Li[1,2,6], Hao-Long Zhou[3,6], Hui Wu[4], Chaohui He[2], Shun Li[2], Rajamani Krishna[5], Jinping Li[2], Wei Zhou[4*] and Banglin Chen[1*]

There are great challenges in developing efficient adsorbents to replace the currently used and energy-intensive cryogenic distillation processes for olefin/paraffin separation, owing to the similar physical properties of the two molecules. Here we report an ultramicroporous metal–organic framework [$Ca(C_4O_4)(H_2O)$], synthesized from calcium nitrate and squaric acid, that possesses rigid one-dimensional channels. These apertures are of a similar size to ethylene molecules, but owing to the size, shape and rigidity of the pores, act as molecular sieves to prevent the transport of ethane. The efficiency of this molecular sieve for the separation of ethylene/ethane mixtures is validated by breakthrough experiments with high ethylene productivity under ambient conditions. This material can be easily synthesized at the kilogram scale using an environmentally friendly method and is water-stable, which is important for potential industrial implementation. The strategy of using highly rigid metal–organic frameworks with well defined and rigid pores could also be extended to other porous materials for chemical separation processes.

Ethylene/ethane separation is a critical process in the petrochemical industry, giving a worldwide ethylene production exceeding 150 million metric tons in 2016. Owing to the very similar sizes and volatilities of these hydrocarbon molecules, the purification of ethylene is currently accomplished by repeated distillation–compression cycling of the mixture under harsh conditions in a huge splitter column of 120–180 trays. This well established industrial separation technology is one of the most energy-intensive processes in the chemical industry; it relies highly on thermal energy and consumes ten times more energy than membrane-based separation technologies or other non-thermal ones[1,2]. It is estimated that, compared to conventional splitters, these advanced non-thermal separation technologies can save the process energy of up to 0.3–1.5 GJ per metric ton of ethylene[3]. To replace the cryogenic distillation processes, exploration of new adsorptive separation technologies based on porous materials is strongly motivated by the tremendous energy savings. As customizable porous materials, metal–organic frameworks (MOFs) are highly versatile in pore engineering, affording precise tuning and functionalization of the pore structure[4,5], and thus have been intensively investigated as excellent adsorbents for selective gas separation[6–13]. However, for ethylene/ethane separation, the major barrier to improving the selectivity for separating these gases is their very similar physical properties. Various functionalized MOF adsorbents, including those featuring open metal sites that help to enhance the olefin binding affinity, have been explored to overcome this challenge[14,15]. However, their co-adsorption of analogous alkanes is inevitable and unfavourable for efficient olefin purification via swing adsorption or membrane-based methods, let alone other problems associated with active metal sites involving the recovery of adsorbent and olefin products (high energy consumption and possible olefin polymerization)[16,17] and water/humidity stability issues.

Ideal separation approaches such as molecular sieving, which allow the complete separation of one component from others based on molecular size or shape cut-off, avoid the co-adsorption of impurities without sacrificing the valuable uptake capacity of porous media and enable infinite selectivity, which is also beneficial to membrane-based separation[18,19]. Accordingly, precise size/shape-matching is vital towards specific recognition of olefin/paraffin[20,21]. Considering the even smaller shape difference between ethylene/ethane (only 0.028 nm in kinetic diameter) and their nearly identical physical properties (Supplementary Fig. 1 and Supplementary Table 1), it is particularly challenging to design MOFs as molecular sieves for this gas separation. The existing dynamic nature of organic moieties (for example, freedom of rotation; Supplementary Fig. 2) makes this separation even more challenging, because such a structural feature can readily change the sizes of pore apertures during the sorption process. Extensive research endeavours have been pursued to tailor-make MOFs for specific molecular sieving of some important hydrocarbons[9,10,22,23], but it is yet to be shown that MOFs can sieve ethylene while completely excluding ethane.

During our exploration of MOF candidates with pore aperture sizes of 3.4–4.4 Å constructed from the rigid organic linkers to minimize the linker rotation/vibration, we have targeted a readily available MOF molecular sieve [$Ca(C_4O_4)(H_2O)$] (termed UTSA-280) that features rigid one-dimensional channels, exhibiting molecular size exclusion of ethane from ethylene under ambient conditions. This material exhibits optimal channel spaces that enable recognition of ethylene molecules of high packing intensity and exceptional selectivity with ethylene productivity of 1.86 mol kg^{-1} under ambient conditions, as has been established by the experimental breakthrough curves. Its straightforward synthesis at a large scale under an environmentally friendly condition, and its water-stability, highlight the promise of this molecular sieving material for industrial C_2H_4/C_2H_6 separation in the future.

Pore structure and single-gas sorption isotherm

Using the common chemical raw materials calcium nitrate and squaric acid, $[Ca(C_4O_4)(H_2O)]\bullet xH_2O$ was synthesized under mild

[1]Department of Chemistry, University of Texas at San Antonio, San Antonio, TX, USA. [2]Research Institute of Special Chemicals, Taiyuan University of Technology, Taiyuan, China. [3]School of Physical Science and Technology, ShanghaiTech University, Shanghai, China. [4]NIST Center for Neutron Research, National Institute of Standards and Technology, Gaithersburg, MD, USA. [5]Van't Hoff Institute for Molecular Sciences, University of Amsterdam, Amsterdam, the Netherlands. [6]These authors contributed equally: Rui-Biao Lin, Libo Li, Hao-Long Zhou. *e-mail: wzhou@nist.gov; banglin.chen@utsa.edu

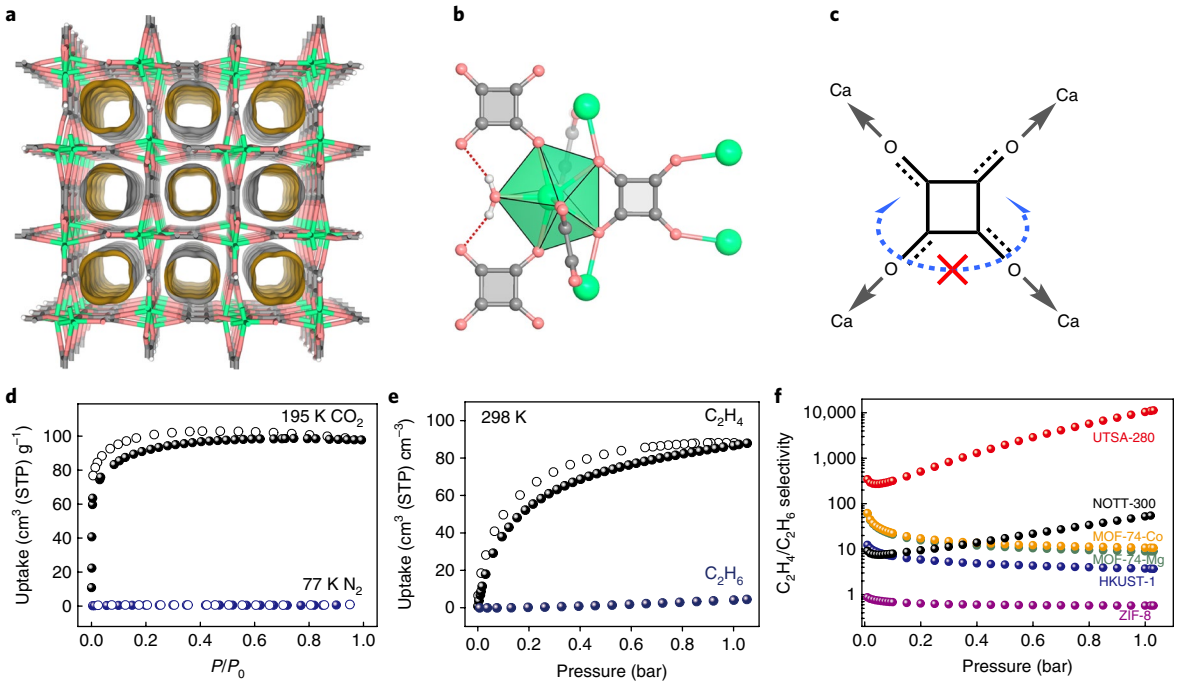

Fig. 1 | Structure and gas sorption properties of UTSA-280. a, The crystal structure of guest-free UTSA-280 determined from single-crystal X-ray diffraction, showing one-dimensional channels viewed along the [001] direction. Green, light coral and grey nodes represent Ca, O and C atoms, respectively. **b**, The local coordination environments of the squarate linker and calcium atoms. **c**, A schematic diagram showing the coordination constraints applied on the $C_4O_4^{2-}$ linker. **d**, **e**, Single-component sorption isotherms of carbon dioxide (black) at 195 K, nitrogen (blue) at 77 K (**d**) and ethylene (black), ethane (indigo) at 298 K for UTSA-280 (**e**). **f**, Qualitative comparison of IAST adsorption selectivities of different MOFs for an equimolar ethylene/ethane mixture at 298 K.

conditions in water (Supplementary Figs. 3 and 4)[24]. In the as-synthesized UTSA-280⊃H_2O, the pentagonal bipyramidal Ca atom is coordinated by seven O atoms from five different $C_4O_4^{2-}$ linkers and one water molecule, bridged by the organic linkers to form one-dimensional infinite chains, resulting in one-dimensional channels occupied by guest water molecules (Fig. 1a). The hydrogen bonding between the coordinated H_2O molecules and the O atoms of the $C_4O_4^{2-}$ linkers further stabilizes the framework (Supplementary Fig. 5). Notably, the $C_4O_4^{2-}$ linkers are subject to mutual coordination constraints from two different calcium-oxo chains, as they coordinate to Ca atoms in different directions that are perpendicular to each other (Fig. 1b), which can effectively restrain the rotations of the organic linkers (Fig. 1c). After removing the guest water molecules, the framework of activated UTSA-280 is fully maintained, as determined by single-crystal X-ray diffraction experiments (Fig. 1 and Supplementary Table 2). The coordinated H_2O molecule is retained in the structure. One-dimensional open cylindrical channels are obtained after guest removal, showing aperture sizes with slightly different shapes of 3.2 × 4.5 Å^2 and 3.8 × 3.8 Å^2 (Fig. 1a). These apertures display similar cross-sectional areas of about 14.4 Å^2, which are larger than the minimum cross-sectional area of C_2H_4 (13.7 Å^2) but smaller than that of C_2H_6 (15.5 Å^2)[25], suggesting great size/shape sieving potential for C_2H_4/C_2H_6 separation. The total solvent-accessible volume was estimated to be 27.8% of the unit-cell volume. While UTSA-280 is remarkably stable in water (Supplementary Fig. 3), we note that the existence of the coordinated water molecules is essential for guest-free UTSA-280 to display permanent porosity. The activation of UTSA-280⊃H_2O should be performed under relatively mild conditions (see Supplementary Information) to retain the coordinated water. The Brunauer–Emmett–Teller surface area of activated UTSA-280 was measured to be ~331 m^2 g^{-1} (Langmuir surface area: ~455 m^2 g^{-1}) by CO_2 sorption experiment at 195 K (Fig. 1d and Supplementary Fig. 6). The experimental total pore volume is ~0.18 cm^3 g^{-1}, matching well with the theoretical one calculated from the crystal structure (0.18 cm^3 g^{-1}).

Pure-component equilibrium adsorption isotherms for C_2H_4 and C_2H_6 were collected at ambient conditions. Figure 1e shows the data obtained at 298 K. The C_2H_4 uptake in UTSA-280 reaches 88.1 cm^3 cm^{-3} (2.5 mmol g^{-1}) at 298 K and 1 bar, higher than those of the benchmark zeolites that are widely studied for ethylene/ethane separation, such as zeolite 5A and cation-exchanged ETS-10 (Engelhard Titanosilicate-10) (1.0–2.3 mmol g^{-1})[26,27]. In contrast, under the same conditions, UTSA-280 adsorbs a negligible amount of ethane (0.098 mmol g^{-1}), which means that the ethane molecule is excluded by the pore apertures, consistent with our structural pore size analysis. At lower temperature (273 K), while a larger C_2H_4 uptake can be observed, there is still no uptake increase for C_2H_6 (Supplementary Fig. 7). This remains true even at 195 K. Notably, according to the amount of adsorbed C_2H_4 and the pore volume, the density of C_2H_4 in the pore channel at room temperature is up to 389 g l^{-1}, which is about 342 times the gaseous C_2H_4 density of 1.138 g l^{-1} (298 K, 1 bar) and close to the liquid C_2H_4 density of 568 g l^{-1} (169.4 K, 1 bar), implying highly efficient packing of ethylene molecules in UTSA-280. From the measured isotherms, record-high apparent C_2H_4/C_2H_6 selectivity, exceeding 10,000 (Fig. 1f, Supplementary Fig. 8 and Supplementary Table 3), can be calculated for the qualitative comparison, which is orders of magnitude larger than those of FeMOF-74 (13.6)[7], NOTT-300 (48.7)[8], π-complexation sorbents[28], such as PAF-1-SO_3Ag (27)[29], and so on (Supplementary Table 4)[30]. However, it should be noted that such calculated selectivity is often subject to uncertainties owing to the large error from the ultralow apparent C_2H_6 uptake. Theoretically, the C_2H_4/C_2H_6 selectivity of UTSA-280 should be infinite, which is promising for molecular exclusion of ethane from ethylene. Subsequently, multiple cycling sorption measurements were conducted carefully to test the material cyclability, showing no

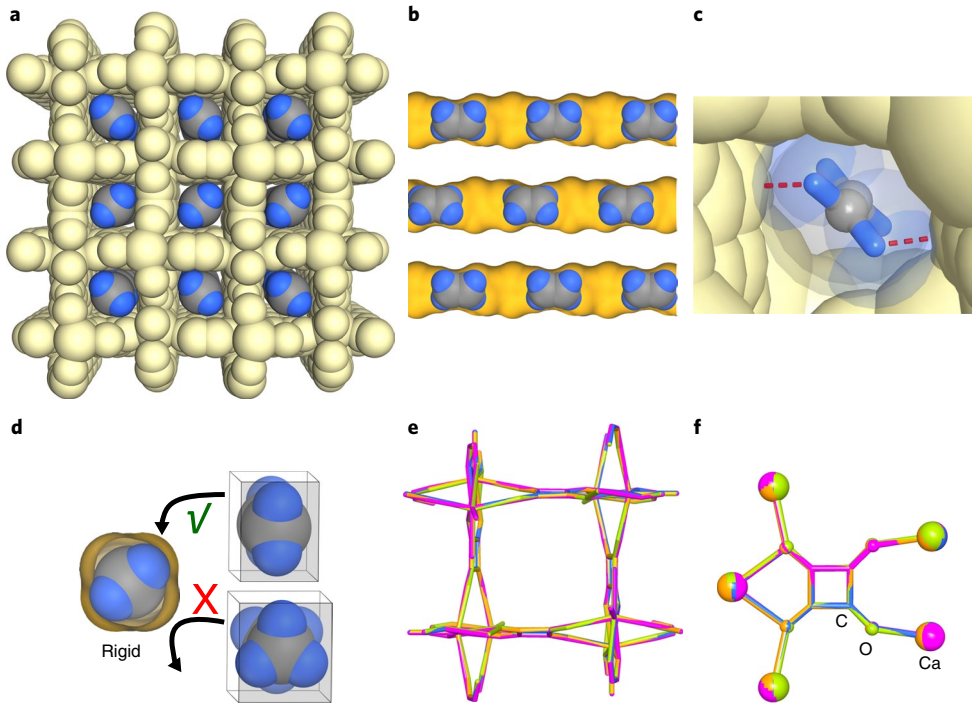

Fig. 2 | Single-crystal structure of UTSA-280•0.20C_2H_4 and preferential C_2H_4 binding. a, **b**, Top and side views of the packing diagram of the C_2H_4 adsorbed structure. The framework and pore surface are shown in pale gold and orange. The light blue and grey spheres represent H and C atoms of C_2H_4 molecules. **c**, Preferential binding site for C_2H_4 molecules and their close contacts with the framework. **d**, Schematic diagram of the size/shape sieving based on the minimum cross-sectional areas of C_2H_4 and C_2H_6 molecules. **e**, **f**, Conformational comparisons of the pore structures (**e**) and $C_4O_4^{2-}$ linkers (**f**) in the single-crystal structures of UTSA-280•H_2O (lime), UTSA-280 (pink), UTSA-280•0.16C_2H_4 (light orange) and UTSA-280•0.20C_2H_4 (light blue).

C_2H_6 adsorption and no loss of C_2H_4 uptake capacity in UTSA-280 (Supplementary Figs. 9–13).

The coverage-dependent isosteric heat of adsorption (Q_{st}) for ethylene was estimated on the basis of the Clausius–Clapeyron equation (Supplementary Fig. 14). The experimental Q_{st} value for C_2H_4 (ranging from 20.5 to 35.0 kJ mol^{-1}) in UTSA-280 was found to be markedly lower than those of many efficient C_2H_4 sorbents (Supplementary Table 4), such as MOFs functionalized with open metal sites (40–85 kJ mol^{-1})[7,31] and π-complexation sorbents (60–120 kJ mol^{-1})[29,32]. Such a low apparent adsorption enthalpy implies the potential to regenerate this MOF under mild conditions, thus avoiding C_2H_4 oligomerization/polymerization that may happen following the catalysis of open metal sites[16,17].

Sieving mechanism and breakthrough separation

Presumably, the main host–guest interactions between C_2H_4 and UTSA-280 are C–H···π and C–H···O interactions, which usually have an important role in protein folding and molecular recognition. To determine the nature of the interactions of C_2H_4 molecules within UTSA-280 structurally, single-crystal X-ray diffraction experiments were carried out. Data for UTSA-280•0.2C_2H_4 were collected at room temperature on a C_2H_4-loaded sample (Fig. 2 and Supplementary Table 2). Non-hydrogen atoms of the adsorbate can be located by employing this technique. Following the C_2H_4 loading, the framework of [Ca(C_4O_4)(H_2O)]•0.2C_2H_4 retains the same as the synthesized and activated ones, while remarkable intensity increases in residual electron density peaks ($F_o - F_c$ contoured raising to 1.9 e Å^{-3} in UTSA-280•0.2C_2H_4) were clearly observed within the cylindrical channel, demonstrating the presence of C_2H_4 molecules (Supplementary Fig. 15). A single crystallographic type of adsorbed C_2H_4 molecule can be successfully located in the middle of the channel from dispersed electron density peaks (Fig. 2a, b and Supplementary Figs. 16 and 17). The refined C_2H_4 shows two-fold disordering over two sites with partial occupancy, which oriented linearly with its C=C axis along the channel and tilted with its minimum cross-section along the diagonal of the pore aperture. The orientation of C_2H_4 molecules inside the channels can minimize any possible steric hindrance and electrostatic repulsion from the framework. Weak C–H···O hydrogen bonding (3.32–3.44 Å), π···π stacking (3.31 Å) and van der Waals (vdW) interactions (shortest C–H···π distance of 3.32 Å) are found between discrete C_2H_4 molecules and the aromatic rings of the $C_4O_4^{2-}$ ligand or coordinated water molecules (Fig. 2c), which are significantly larger than those observed in MOFs with strong binding sites (for example, 2.42 Å for C_2H_4 with the open Fe site in Fe-MOF-74)[7], being consistent with its lower adsorption enthalpy. Considering the vdW radii of atoms, the tilted C_2H_4 molecule fits the narrow pore channel well (Fig. 2d). In contrast, owing to the cross-section being larger (15.5 Å^2) than the pore aperture (14.4 Å^2), significant steric hindrance is unavoidable when a C_2H_6 molecule of staggered conformation is put inside the channels with whichever orientations, which is well confirmed by the calculated potential energy variation of C_2H_6 along the pore channel (Supplementary Fig. 18). Importantly, structural comparison of UTSA-280 with different guest inclusions shows that the pore structure is basically not changed (Fig. 2e), in which no conformation change or abnormal atomic displacement parameter is observed for the $C_4O_4^{2-}$ linker (Fig. 2f and Supplementary Figs. 5, 16 and 17), confirming a relatively high degree of pore and framework rigidity. This rigidity is also supported by additional diffraction data for UTSA-280 under various other external stimuli, including temperature variation (Supplementary Figs. 19–22). Therefore, the pore aperture size is unlikely to become large enough to accommodate C_2H_6 molecules during the sorption process. Overall, the specific C_2H_4 adsorption is because C_2H_4 molecules can diffuse into the confined channel utilizing its optimal orientation, while C_2H_6 molecules are subject to the inaccessibility of this rigid pore channel.

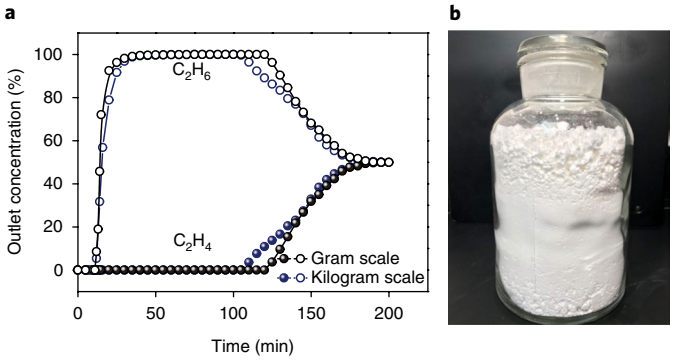

Fig. 3 | Column breakthrough results and scalable synthesis of UTSA-280. a, Breakthrough curves for UTSA-280 from different scales for an equimolar binary mixture of C_2H_4/C_2H_6 at 298 K and 1 bar. The breakthrough experiments were carried out in a packed column with 3.2 g sample at a flow rate of 2 ml min^{-1}. The points are experimental data, and the lines are drawn to guide the eye. **b**, 0.22 kg synthesis of UTSA-280⊃H_2O obtained from rapid mixing of a saturated aqueous solution of sodium squarate with an aqueous solution of calcium nitrate.

On the basis of the gas-loaded structure, we performed first-principles dispersion-corrected density functional theory (DFT) calculations to further confirm the C_2H_4 adsorption nature in UTSA-280. We found that the calculated C_2H_4 adsorption location and orientation are consistent with the experimental results from the diffraction data (Supplementary Fig. 23). Moreover, the adsorbed C_2H_4 molecule interacts with the surrounding channel surface through π···π stacking (3.31 Å) and vdW interactions with the aromatic rings of the $C_4O_4^{2-}$ linkers. Overall, the adsorption interaction is a weak dispersive interaction in nature. The dispersion-corrected DFT-calculated static binding energy is quite modest, ~37.8 kJ mol^{-1}, and consistent with the relatively low isosteric heat (34.1 kJ mol^{-1}) observed experimentally in UTSA-280. Overall, such molecular exclusion of ethane from ethylene associated with low binding affinity indicates that UTSA-280 can serve as a promising molecular sieve for ethylene enrichment.

In the common process for ethylene production based on the cracking of heavier hydrocarbon fractions, followed by dehydrogenation reactions, the conversion yield of the later step is only around 50–60%[33]. Other processes such as catalytic dehydrogenation also give an equimolar mixture of C_2H_4 and C_2H_6. Thus, the upgrading of ethylene from the C_2H_4/C_2H_6 mixture is a very important process before further utilization. Although certain molecular exclusions can also be achieved on a few flexible porous materials[34,35], the co-adsorption of other impurities during the opening of the pore structure makes their column breakthrough separation very tough, giving low-purity ethylene. To evaluate the performance of UTSA-280 in an adsorptive dynamic separation process, breakthrough experiments were performed, in which an equimolar C_2H_4/C_2H_6 mixture was flowed over a packed column of the activated solid with a rate of 2 ml min^{-1} at 298 K (Fig. 3a and Supplementary Fig. 24). As expected, clean separation of the challenging C_2H_4/C_2H_6 mixture was realized by using UTSA-280. C_2H_6 was first to elute through the bed, and then the outlet gas quickly reached pure grade with no detectable C_2H_4 (below the detection limit of the experimental setup), whereas the solid adsorbent retained C_2H_4 for a remarkable time before the breakthrough of C_2H_4. Hence, C_2H_6 can be removed from C_2H_4 with no loss of valuable C_2H_4, which is in line with the sorption experiments. The amount of C_2H_4 enriched from the equimolar C_2H_4/C_2H_6 mixture was up to 1.86 mol kg^{-1} (Supplementary Fig. 25), which is slightly lower than the equilibrium capacity of UTSA-280 at 0.5 bar (2.05 mol kg^{-1}) owing to the relatively slow diffusion of C_2H_4 into this MOF during the separation process (Supplementary Fig. 26). It can be further increased at higher pressures (Supplementary Fig. 27). Enriched C_2H_4 can then be recovered with high purity during the regeneration step, which was carried out by applying a vacuum (Supplementary Fig. 28). Moreover, regeneration of UTSA-280 under a He flow at 353 K revealed that the adsorbed gas can be completely recovered within 10 min (Supplementary Fig. 29), which is significantly faster than that of Ag-doped adsorbent (up to thousands of minutes)[29]. These results demonstrate that the challenging C_2H_6 removal can be satisfactorily addressed under mild conditions (1–2 bar, 298 K), considering that the realistic pressure of cracked gas steam leaving from the thermal cracking furnace is ~1.55 bar (ref. [36]). For benchmark zeolites with a small pore aperture for the kinetic separation, similar separation has been realized at 8.5 bar and 323 K (ref. [30]). Multiple cycling breakthrough experiments under the aforementioned operating conditions show the same retention time as the initial one, which revealed that UTSA-280 maintained its ethylene uptake capacity and molecular exclusion of ethane (Supplementary Fig. 30). For comparison with breakthrough experiments of UTSA-280, transient breakthrough simulation was also carried out (Supplementary Fig. 31), which was found to be certainly consistent with the experimental results.

Effect of gas impurity on ethylene production

Besides the separation of C_2H_4 from C_2H_6, there is tremendous current interest in the recovery of valuable ethylene from refinery gas streams (typically consisting of 51% methane, 21.4% ethylene, 21.1% ethane and 6.5% propane)[28,37], which are usually used as fuel gas. An adsorptive separation process that uses this molecular sieve for the recovery of C_2H_4 from similar mixtures could potentially result in substantial economic benefits. To evaluate the feasibility of using UTSA-280 for this task, we carried out breakthrough experiments for a quaternary $CH_4/C_2H_4/C_2H_6/C_3H_8$ mixture (45/25/25/5). On the basis of the sieving effect (Fig. 4a), specific C_2H_4 enrichment from the above quaternary gas mixture was realized with UTSA-280 (Supplementary Fig. 32). It should be noted that the realistic gas stream in ethylene plants is more complex; for example, a typical steam from ethane cracking contains 3.7–4.2% H_2, 3.7–5.4% CH_4, 0.3–1.2% C_2H_2, 45.7–49.7% C_2H_4, 32.7–41.3% C_2H_6, 0.8–1.5% C_3H_6, 0.2–0.3% C_3H_8 and 0.3–0.8% C_4H_8 (ref. [36]). Consequently, we have carried out breakthrough experiments for an octonary $H_2/CH_4/C_2H_2/C_2H_4/C_2H_6/C_3H_6/C_3H_8/C_4H_8$ mixture (4/5/1/45/40/2/1/2), which also demonstrates that this MOF is competent to exclusively enrich C_2H_4 from the complicated cracking stream (Fig. 4b).

Scalable synthesis and stability

Among reported MOFs for C_2H_4/C_2H_6 separation, MOFs with open metal sites are indeed efficient at capturing C_2H_4 via strong coordination interactions, which can produce very high C_2H_4 uptake at ambient conditions. However, MOFs with open metal sites are

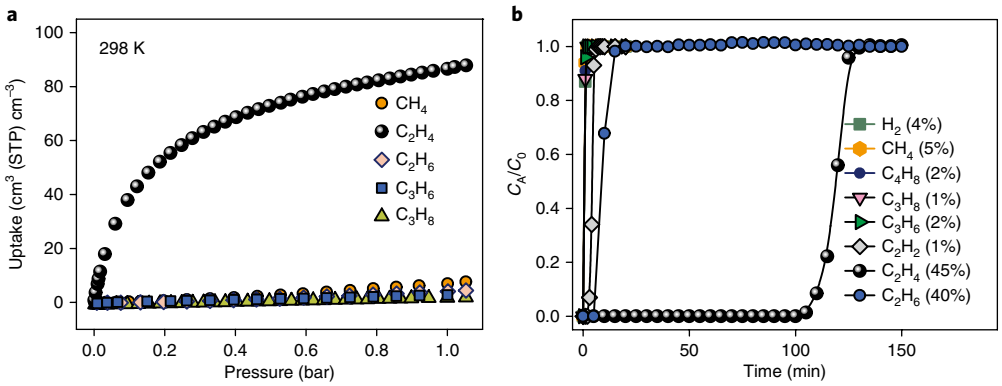

Fig. 4 | Separation performance of UTSA-280 for a gas mixture containing C_2H_4. a, Single-component adsorption isotherms of CH_4 (orange circles), C_2H_4 (black circles), C_2H_6 (pink diamonds), C_3H_6 (blue squares) and C_3H_8 (lime triangles) in UTSA-280 at 298 K. **b**, Multi-component breakthrough curves for an octonary mixture of $H_2/CH_4/C_2H_2/C_2H_4/C_2H_6/C_3H_6/C_3H_8/C_4H_8$ (4/5/1/45/40/2/1/2) at 298 K and 1 bar. The breakthrough experiments were carried out in a packed column at a flow rate of 2 ml min^{-1}. The points are experimental data, and the lines are drawn to guide the eye.

highly sensitive to moisture owing to their preferred coordination with water, resulting in a significantly reduced C_2H_4 uptake capacity and/or binding affinity. In contrast, UTSA-280 is stable in water (Supplementary Fig. 33) as demonstrated by powder X-ray diffraction patterns of the sample after immersion in water for days. Moreover, gas sorption experiments of the reactivated UTSA-280 from the water-treated and moisture-exposed samples revealed that this material still maintains the same sorption performance for C_2H_4 (Supplementary Fig. 34), indicating that UTSA-280 is water-stable[38]. As shown in Supplementary Figs. 35–37, further breakthrough experiments and selectivity calculations under moisture (10 to 1,137 parts per million H_2O) also demonstrate that UTSA-280 can maintain its separation performance under more extreme conditions than would be found in a realistic process[10]. Such properties are apparently important for its potential industrial application. Furthermore, UTSA-280 is easily synthesized from very common chemical commodities via a 'green' and scalable method at room temperature (Fig. 3b and Supplementary Fig. 38), in which the only solvent is water. Overall, by virtue of the optimal and rigid pore channel of a known, water-stable, ultramicroporous MOF made by an environmentally friendly method, molecular exclusion of ethane from ethylene has been realized for promising energy-efficient separation technologies.

Outlook

Optimal pore size and suitable functionality are essential features enabling porous materials to address key challenging gas separations. The above results illustrate that the ideal molecular exclusion of ethane from ethylene can be readily achieved by integrating the merits of size/shape match and high rigidity into the pore structure, which may greatly facilitate the very challenging membrane-based separation of such essential hydrocarbons. In principle, pore engineering in MOF chemistry is generally applicable to other types of porous material including porous organic polymers, covalent organic frameworks and hydrogen-bonded organic frameworks. A detailed examination of the pore features in various porous materials will be needed for the discovery of other molecular sieves in the future, and thus broaden the exploration of separation technologies with energy-efficient prospects, affording tremendous opportunity for valuable gas separations.

Online content

Any methods, additional references, Nature Research reporting summaries, source data, statements of data availability and associated accession codes are available at https://doi.org/10.1038/s41563-018-0206-2.

Received: 22 March 2018; Accepted: 25 September 2018;
Published online: 5 November 2018

References

1. Sholl, D. S. & Lively, R. P. Seven chemical separations to change the world. *Nature* **532**, 435–437 (2016).
2. Chu, S., Cui, Y. & Liu, N. The path towards sustainable energy. *Nat. Mater.* **16**, 16–22 (2017).
3. Ren, T., Patel, M. & Blok, K. Olefins from conventional and heavy feedstocks: energy use in steam cracking and alternative processes. *Energy* **31**, 425–451 (2006).
4. Kitagawa, S. Porous materials and the age of gas. *Angew. Chem. Int. Ed.* **54**, 10686–10687 (2015).
5. Furukawa, H., Cordova, K. E., O'Keeffe, M. & Yaghi, O. M. The chemistry and applications of metal–organic frameworks. *Science* **341**, 1230444 (2013).
6. Matsuda, R. et al. Highly controlled acetylene accommodation in a metal–organic microporous material. *Nature* **436**, 238–241 (2005).
7. Bloch, E. D. et al. Hydrocarbon separations in a metal–organic framework with open iron(II) coordination sites. *Science* **335**, 1606–1610 (2012).
8. Yang, S. et al. Supramolecular binding and separation of hydrocarbons within a functionalized porous metal–organic framework. *Nat. Chem.* **7**, 121–129 (2014).
9. Cadiau, A., Adil, K., Bhatt, P. M., Belmabkhout, Y. & Eddaoudi, M. A metal–organic framework-based splitter for separating propylene from propane. *Science* **353**, 137–140 (2016).
10. Cui, X. et al. Pore chemistry and size control in hybrid porous materials for acetylene capture from ethylene. *Science* **353**, 141–144 (2016).
11. Liao, P.-Q., Huang, N.-Y., Zhang, W.-X., Zhang, J.-P. & Chen, X.-M. Controlling guest conformation for efficient purification of butadiene. *Science* **356**, 1193–1196 (2017).
12. Yoon, J. W. et al. Selective nitrogen capture by porous hybrid materials containing accessible transition metal ion sites. *Nat. Mater.* **16**, 526–531 (2016).
13. Vaidhyanathan, R. et al. Direct observation and quantification of CO_2 binding within an amine-functionalized nanoporous solid. *Science* **330**, 650–653 (2010).
14. He, Y., Krishna, R. & Chen, B. Metal–organic frameworks with potential for energy-efficient adsorptive separation of light hydrocarbons. *Energy Environ. Sci.* **5**, 9107–9120 (2012).
15. Zhai, Q.-G. et al. An ultra-tunable platform for molecular engineering of high-performance crystalline porous materials. *Nat. Commun.* **7**, 13645 (2016).
16. Ji, P. et al. Transformation of metal–organic framework secondary building units into hexanuclear Zr-alkyl catalysts for ethylene polymerization. *J. Am. Chem. Soc.* **139**, 11325–11328 (2017).
17. Klet, R. C. et al. Single-site organozirconium catalyst embedded in a metal–organic framework. *J. Am. Chem. Soc.* **137**, 15680–15683 (2015).
18. Lin, J. Y. S. Molecular sieves for gas separation. *Science* **353**, 121–122 (2016).
19. Peng, Y. et al. Metal–organic framework nanosheets as building blocks for molecular sieving membranes. *Science* **346**, 1356–1359 (2014).
20. Pan, L., Olson, D. H., Ciemnolonski, L. R., Heddy, R. & Li, J. Separation of hydrocarbons with a microporous metal–organic framework. *Angew. Chem. Int. Ed.* **45**, 616–619 (2006).

21. Ma, S., Sun, D., Yuan, D., Wang, X. & Zhou, H. Preparation and gas adsorption studies of three mesh-adjustable molecular sieves with a common structure. *J. Am. Chem. Soc.* **131**, 6445–6451 (2009).
22. Bao, Z. et al. Potential of microporous metal–organic frameworks for separation of hydrocarbon mixtures. *Energy Environ. Sci.* **9**, 3612–3641 (2016).
23. Adil, K. et al. Gas/vapour separation using ultra-microporous metal–organic frameworks: insights into the structure/separation relationship. *Chem. Soc. Rev.* **46**, 3402–3430 (2017).
24. Robl, C. & Weiss, A. Alkaline-earth squarates III. $CaC_4O_4{\cdot}2.5H_2O$, a novel polymer complex with zeolitic properties (1). *Mater. Res. Bull.* **22**, 373–380 (1987).
25. Webster, C. E., Drago, R. S. & Zerner, M. C. Molecular dimensions for adsorptives. *J. Am. Chem. Soc.* **120**, 5509–5516 (1998).
26. Mofarahi, M. & Salehi, S. M. Pure and binary adsorption isotherms of ethylene and ethane on zeolite 5A. *Adsorption* **19**, 101–110 (2013).
27. Anson, A., Wang, Y., Lin, C. C. H., Kuznicki, T. M. & Kuznicki, S. M. Adsorption of ethane and ethylene on modified ETS-10. *Chem. Eng. Sci.* **63**, 4171–4175 (2008).
28. Yang, R. T. *Adsorbents: Fundamentals and Applications* (John Wiley & Sons, Hoboken, 2003).
29. Li, B. et al. Introduction of π-complexation into porous aromatic framework for highly selective adsorption of ethylene over ethane. *J. Am. Chem. Soc.* **136**, 8654–8660 (2014).
30. Bereciartua, P. J. et al. Control of zeolite framework flexibility and pore topology for separation of ethane and ethylene. *Science* **358**, 1068–1071 (2017).
31. Yoon, J. W. et al. Controlled reducibility of a metal–organic framework with coordinatively unsaturated sites for preferential gas sorption. *Angew. Chem. Int. Ed.* **49**, 5949–5952 (2010).
32. Aguado, S., Bergeret, G., Daniel, C. & Farrusseng, D. Absolute molecular sieve separation of ethylene/ethane mixtures with silver zeolite A. *J. Am. Chem. Soc.* **134**, 14635–14637 (2012).
33. Faiz, R. & Li, K. Olefin/paraffin separation using membrane based facilitated transport/chemical absorption techniques. *Chem. Eng. Sci.* **73**, 261–284 (2012).
34. Sen, S. et al. Cooperative bond scission in a soft porous crystal enables discriminatory gate opening for ethylene over ethane. *J. Am. Chem. Soc.* **139**, 18313–18321 (2017).
35. Kishida, K. et al. Recognition of 1,3-butadiene by a porous coordination polymer. *Angew. Chem. Int. Ed.* **55**, 13784–13788 (2016).
36. Sadrameli, S. M. Thermal/catalytic cracking of hydrocarbons for the production of olefins: a state-of-the-art review I: thermal cracking review. *Fuel* **140**, 102–115 (2015).
37. Zhang, Y., Wu, J.-h & Zhang, D.-k Cracking of simulated oil refinery off-gas over a coal char, petroleum coke, and quartz. *Energy Fuels* **22**, 1142–1147 (2008).
38. Horike, S. et al. Postsynthesis modification of a porous coordination polymer by LiCl to enhance H^+ transport. *J. Am. Chem. Soc.* **135**, 4612–4615 (2013).

Acknowledgements

This work was supported by grant AX-1730 from the Welch Foundation (B.C.), the National Natural Science Foundation of China (grant 21606163) and the Natural Science Foundation of Shanxi (grant 201601D021042).

Author contributions

R.-B.L., W.Z. and B.C. conceived the research idea and designed the experiments. R.-B.L., L.L. and H.-L.Z. performed the experiments and analysed data. H.-L.Z. participated in the structural determination of MOFs. R.K. performed the simulations of mixture separations. L.L., C.H., S.L. and J.L. participated in the breakthrough measurement. H.W. and W.Z. did the DFT calculation. R.-B.L., W.Z. and B.C. discussed and co-wrote the paper. All authors discussed the results and commented on the manuscript. R.-B.L., L.L. and H.-L.Z. contributed equally to this work.

Competing interests

The authors declare no competing interests.

Additional information

Supplementary information is available for this paper at https://doi.org/10.1038/s41563-018-0206-2.

Reprints and permissions information is available at www.nature.com/reprints.

Correspondence and requests for materials should be addressed to W.Z. or B.C.

Publisher's note: Springer Nature remains neutral with regard to jurisdictional claims in published maps and institutional affiliations.

Methods

Materials. Calcium nitrate tetrahydrate ($Ca(NO_3)_2$•$4H_2O$, 99%, Fisher Chemical), sodium hydroxide (NaOH, 98%, Alfa Aesar), glacial acetic acid ($C_2H_4O_2$, 99.7%, Fisher Chemical) and squaric acid (or 3,4-dihydroxycyclobut-3-ene-1,2-dione, $C_4H_2O_4$, 99.0%, Oakwood Chemicals) were purchased and used without further purification.

N_2 (99.999%), CO_2 (99.999%), C_2H_4 (99.5%), C_2H_6 (99.5%) and He (99.999%) were purchased from Airgas. Mixed gases including C_2H_4/C_2H_6 = 50/50 (vol/vol), $CH_4/C_2H_4/C_2H_6/C_3H_8$ = 45/25/25/5 (vol/vol/vol/vol) and $H_2/CH_4/C_2H_2/C_2H_4/C_2H_6/C_3H_6/C_3H_8/C_4H_8$ = 4/5/1/45/40/2/1/2 (vol/vol/vol/vol/vol/vol/vol/vol) were purchased from Beijing Special Gas Co. Ltd.

Synthesis of $[Ca(C_4O_4)(H_2O)]$•xH_2O. The synthesis of the single-crystal sample was performed following a reported method with minor modifications[24]. A solution of squaric acid (182 mg, 1.6 mmol) and NaOH (3.2 mmol, 128 mg) in 16 ml water was carefully layered on a solution of $Ca(NO_3)_2$•$4H_2O$ (8.0 mmol, 1.888 g), CH_3COOH (2.75 ml, 2.882 g) and NaOH (32 mmol, 1.280 g) in 40 ml water. Colourless single crystals of $[Ca(C_4O_4)(H_2O)]$•xH_2O were obtained in a few days. The resultant crystals were filtered, washed thoroughly with water and dried under air, with yields of 61% based on squaric acid. A microcrystalline powder sample was obtained by mixing a saturated aqueous solution (10 ml) of sodium squarate ($Na_2C_4O_4$, 1 mmol, 0.158 g) with an aqueous solution (10 ml) of $Ca(NO_3)_2$•$4H_2O$ (5 mmol, 1.180 g). Microcrystalline powders came out immediately and the reaction completely finished within a few minutes; then, after 10 min at room temperature, the sample was filtered, washed thoroughly with water and dried under air, with a yield of 0.146 g (74% based on sodium squarate).

Large-scale synthesis of $[Ca(C_4O_4)(H_2O)]$•xH_2O. Synthesis at 1,000-times scale was carried out as follows. A microcrystalline powder sample was obtained by mixing a saturated aqueous solution (3.29 l) of sodium squarate ($Na_2C_4O_4$, 1,190 mmol, 0.188 kg) with an aqueous solution (0.6 l) of $Ca(NO_3)_2$•$4H_2O$ (5,950 mmol, 1.404 kg). Microcrystalline powders came out immediately and the reaction completely finished within a few minutes; then, after 10 min at room temperature, the sample was filtered, washed thoroughly with water and dried under air, with a yield of 0.219 kg (93% based on sodium squarate). Depending on the container size, the synthesis scale can be even higher.

Preparation of $[Ca(C_4O_4)(H_2O)]$ (UTSA-280). A single crystal of as-synthesized $[Ca(C_4O_4)(H_2O)]$•xH_2O was sealed in a glass capillary, activated in situ under high vacuum for 24 h at 100 °C, followed at 110 °C for another 48 h. The obtained $[Ca(C_4O_4)(H_2O)]$ crystal was sealed for the X-ray diffraction experiment.

It should be noted that activation at higher temperatures or for longer times would lead to loss of the coordinated water and collapse of the crystalline framework structure, and thus the loss of molecular sieving capability.

Single-component gas sorption measurement. The gas sorption measurements were prepared according to ref. [39], and reproduced here for completeness. The gas sorption isotherms were collected on an automatic volumetric adsorption apparatus (Micromeritics ASAP 2020 surface area analyser). Before the sorption measurements, the as-synthesized sample was washed with methanol three times and placed in a quartz tube and dried under high vacuum for 36–72 h at 110 °C (depending on the particle sizes) to remove the guest water molecules, giving the activated UTSA-280 for gas sorption analyses.

Breakthrough separation experiments. The breakthrough experiments were carried out in a dynamic gas breakthrough set-up[39]. A stainless-steel column with inner dimensions of 9 mm and a length of 150 mm was used for sample packing. A pelleted microcrystalline sample (3.2 g) with a particle size of 220–320 μm was then packed into the column. The column was placed in a temperature-controlled environment (maintained at 298 K). The mixed gas flow and pressure were controlled by using a pressure controller valve and a mass flow controller. Outlet effluent from the column was continuously monitored using gas chromatography (GC-2014, Shimadzu) with a thermal conductivity detector. The column packed with activated sample was first purged with helium gas flow for 2 h at 373 K. The mixed gas flow rate during the breakthrough process is 2 standard cubic centimetres per minute using different gas mixtures at 1 bar. After the breakthrough experiment, the sample was regenerated with helium gas flow (50 standard cubic centimetres per minute) for about 15 min at 353 K.

X-ray diffraction analysis of powder samples. Powder X-ray diffraction patterns were collected using a Rigaku Ultima IV diffractometer (Cu Kα λ = 1.540598 Å) with an operating power of 40 kV, 44 mA and a scan rate of 8.0° min^{-1}. The data were collected in the range of 2θ = 5–40°. In situ powder X-ray diffraction patterns were collected using a Bruker D8 ADVANCE X-ray diffractometer equipped with an XRK high-temperature chamber and the high vacuum line under an operating power of 40 kV, 40 mA for Cu Kα radiation.

Single-crystal X-ray diffraction experiments. The single crystals of UTSA-280•$0.16C_2H_4$ and UTSA-280•$0.20C_2H_4$ were obtained by loading ethylene gas at about 300 and 600 mmHg and ambient temperature. Diffraction data were collected on a Bruker D8 Venture or Rigaku CCD (charge-coupled device) diffractometer with Cu Kα radiation (λ = 1.54178 Å) at 298 K. Multi-scan absorption corrections were performed with a Bruker APEX III. The structures were solved by the direct method and refined with the full-matrix least-squares technique using the SHELXTL program. For the framework, anisotropic thermal parameters were applied to all non-hydrogen atoms. Hydrogen atoms were generated geometrically. For gas molecules, ethylene was located from the strong electron density peaks and refined with isotropic displacement parameters. The C–C distances were restrained to 1.30(1) for ethylene. Hydrogen atoms on ethylene molecules were added with geometrical constraints. Crystal data for the compounds are summarized in Supplementary Table 2. CCDC 1582383–1582384 and 1855047–1855048 contain the supplementary crystallographic data for UTSA-280, UTSA-280•$0.20C_2H_4$, UTSA-280•$0.16C_2H_4$ and UTSA-280•H_2O, respectively. These data can be obtained free of charge from the Cambridge Crystallographic Data Centre via www.ccdc.cam.ac.uk/data_request/cif.

DFT calculations. The DFT calculations were performed according to ref. [39], and reproduced here for completeness. First-principles DFT calculations were performed using the Quantum-Espresso package[40]. A semiempirical addition of dispersive forces to conventional DFT was included in the calculation to account for vdW interactions[41]. We used Vanderbilt-type ultrasoft pseudopotentials and generalized gradient approximation with a Perdew–Burke–Ernzerhof exchange correlation. A cutoff energy of 544 eV and a 2 × 2 × 4 k-point mesh (generated using the Monkhorst–Pack scheme) were found to be enough for the total energy to converge within 0.01 meV per atom. We first optimized the structure of UTSA-280. A C_2H_4 gas molecule was then introduced to the optimized host structure at the experimentally identified adsorption site, followed by a full structural relaxation. To obtain the gas binding energy, an isolated gas molecule placed in a supercell (with the same cell dimensions as the MOF crystal) was also relaxed as a reference. The static binding energy (at T = 0 K) was then calculated using $\Delta E = E(\text{MOF} + \text{gas molecule}) - E(\text{MOF}) - E(\text{gas molecule})$. A negative ΔE value would mean that the gas adsorption is energetically favourable. Note that in the main text, only the absolute value of ΔE is cited to describe the binding strength.

Fitting of pure-component isotherms. The pure-component isotherm data for C_2H_4 and C_2H_6 in UTSA-280 were fitted with the single-site Langmuir–Freundlich model.

$$N = N_{\max}\frac{b_p{}^{1/n}}{1 + b_p{}^{1/n}} \quad (1)$$

where p (unit: kPa) is the pressure of the bulk gas at equilibrium with the adsorbed phase, N (unit: mmol g^{-1}) is the adsorbed amount per mass of adsorbent, $N^{\max}$ (unit: mmol g^{-1}) is the saturation capacities, b (unit: 1/kPa) is the affinity coefficient and n represents the deviation from an ideal homogeneous surface. The fitted parameter values are presented in Supplementary Table 3.

Isosteric heat of adsorption. The binding energy of C_2H_2 is reflected in the isosteric heat of adsorption, Q_{st}. The Clausius–Clapeyron equation was employed to calculate the enthalpies of C_2H_4 adsorption:

$$\frac{\partial(\ln P)}{\partial(1/_T)} = -\frac{Q_{st}}{R} \quad (2)$$

where P is the pressure, T is the temperature and R is the universal gas constant. Adsorption heats (Q_{st}) of UTSA-280 for ethylene reported here are estimated using pure-component isotherms collected at 273, 298 and 313 K.

IAST calculations of adsorption selectivities. The adsorption selectivity for C_2H_2/C_2H_4 separation is defined by

$$S_{ads} = \frac{q_1/q_2}{p_1/p_2} \quad (3)$$

q_1 and q_2 are the molar loadings in the adsorbed phase in equilibrium with the bulk gas phase with partial pressures p_1 and p_2.

Transient breakthrough of C_2H_2/C_2H_4 mixtures in fixed-bed adsorbers. For comparison with breakthrough experiments with UTSA-280, transient breakthrough simulations were undertaken using the same methodology as discussed in earlier publications[42]. The dimensions of the breakthrough tube, sample mass and flow rates were chosen to precisely match the experimental conditions. The

simulated breakthrough is shown in Supplementary Fig. 20. The breakthrough times of C_2H_6 and C_2H_4 are captured reasonably accurately. The simulated breakthroughs are sharper than those observed experimentally. The reason for this is that in the simulations, intracrystalline diffusional influences are ignored. The distended characteristics of the experimental breakthroughs with UTSA-280 are because of finite diffusional resistances.

We investigated the separation performance of UTSA-280 for separation of a 50/50 C_2H_2/C_2H_4 feed mixture. The total bulk gas phase is at 298 K and 100 kPa.

Data availability

The data that support the plots within this paper and other finding of this study are available from the corresponding authors upon reasonable request.

References

39. Lin, R.-B. et al. Optimized separation of acetylene from carbon dioxide and ethylene in a microporous material. *J. Am. Chem. Soc.* **139**, 8022–8028 (2017).
40. Giannozzi, P. et al. QUANTUM ESPRESSO: a modular and open-source software project for quantum simulations of materials. *J. Phys. Condens. Matter* **21**, 395502 (2009).
41. Barone, V. et al. Role and effective treatment of dispersive forces in materials: Polyethylene and graphite crystals as test cases. *J. Comput. Chem.* **30**, 934–939 (2009).
42. Krishna, R. The Maxwell–Stefan description of mixture diffusion in nanoporous crystalline materials. *Microporous Mesoporous Mater.* **185**, 30–50 (2014).

nature materials

SUPPLEMENTARY INFORMATION

https://doi.org/10.1038/s41563-018-0206-2

In the format provided by the authors and unedited.

Molecular sieving of ethylene from ethane using a rigid metal–organic framework

Rui-Biao Lin[1,6], Libo Li[1,2,6], Hao-Long Zhou[3,6], Hui Wu[4], Chaohui He[2], Shun Li[2], Rajamani Krishna[5], Jinping Li[2], Wei Zhou[4*] and Banglin Chen[1*]

[1]Department of Chemistry, University of Texas at San Antonio, San Antonio, TX, USA. [2]Research Institute of Special Chemicals, Taiyuan University of Technology, Taiyuan, China. [3]School of Physical Science and Technology, ShanghaiTech University, Shanghai, China. [4]NIST Center for Neutron Research, National Institute of Standards and Technology, Gaithersburg, MD, USA. [5]Van't Hoff Institute for Molecular Sciences, University of Amsterdam, Amsterdam, the Netherlands. [6]These authors contributed equally: Rui-Biao Lin, Libo Li, Hao-Long Zhou. *e-mail: wzhou@nist.gov; banglin.chen@utsa.edu

Supplementary Information

Molecular sieving of ethylene from ethane using a rigid metal-organic framework

Rui-Biao Lin,[1†] Libo Li,[1,2†] Hao-Long Zhou,[3†] Hui Wu,[4] Chaohui He,[2] Shun Li,[2] Rajamani Krishna,[5] Jinping Li,[2] Wei Zhou,[4]* Banglin Chen[1]*

[1]*Department of Chemistry, University of Texas at San Antonio, One UTSA Circle, San Antonio, Texas 78249-0698, USA.* [2]*Research Institute of Special Chemicals, Taiyuan University of Technology, Taiyuan 030024, Shanxi, China.* [3]*School of Physical Science and Technology, ShanghaiTech University, Shanghai 201210, China.* [4]*NIST Center for Neutron Research, National Institute of Standards and Technology, Gaithersburg, Maryland 20899-6102, USA.* [5]*Van't Hoff Institute for Molecular Sciences, University of Amsterdam, Science Park 904, 1098 XH Amsterdam, The Netherlands.* *Correspondence to: wzhou@nist.gov; banglin.chen@utsa.edu

Supplementary Figures

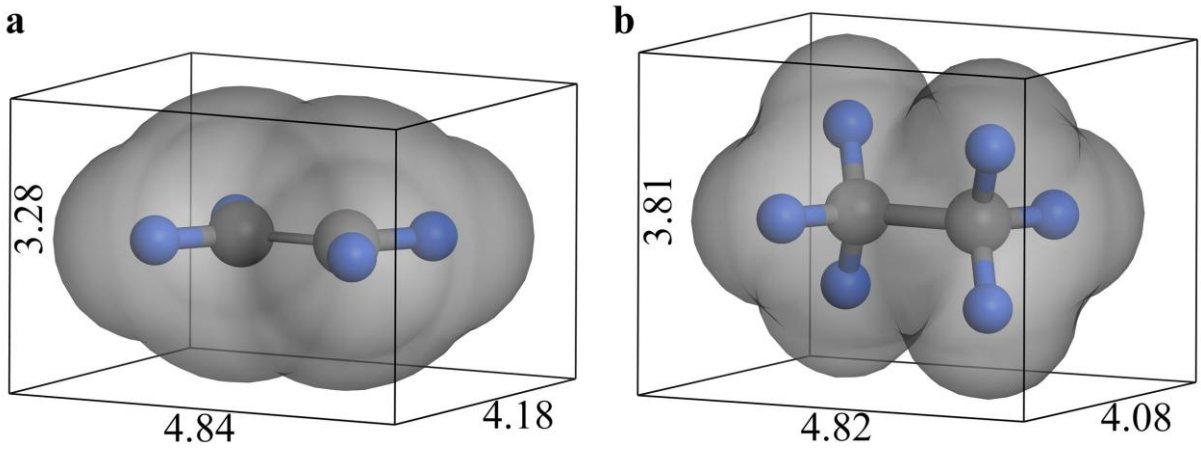

Supplementary Figure 1. Molecular dimensions of ethylene (**a**) and ethane (**b**). The unit of length is angstrom (Å). The dimension of the adsorbate used to evaluate its entry into a pore is related to the shape of the pore. For cylindrical pores/channels, the size of selected molecule in two directions must be taken into account, that is the minimum cross-sectional area [1]. The relevant dimensions are minimum one (MIN-1, e. g. 3.28 Å for ethylene) and the next to the smallest perpendicular distance for low energy conformations or molecular orientations that enable a molecule to enter a cylinder (MIN-2, e.g. 4.18 Å for ethylene). So, the minimum cross-sectional area of ethylene and ethane molecules are 13.7 (3.28 Å × 4.18 Å) and 15.5 (3.81 Å × 4.08 Å) $Å^2$, respectively, which should be taken into account when evaluating their entry into a narrow cylindrical pore.

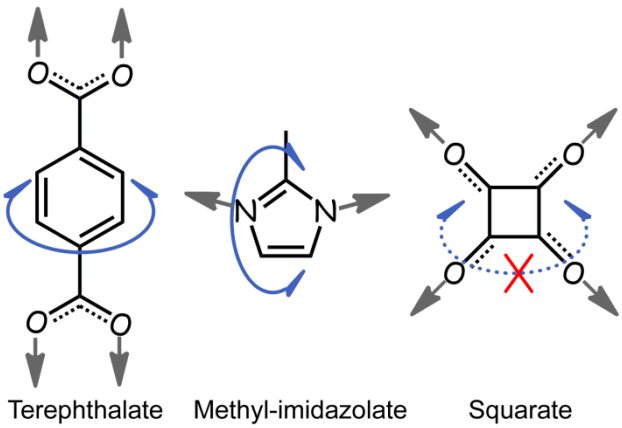

Supplementary Figure 2. The schematic diagram shows the dynamic nature of organic moieties in MOF-5 (e.g. *J. Am. Chem. Soc., 130, 3246-3247, 2008*), ZIF-8 (e.g. *Chem. Commun., 48, 11395–11397, 2012*) and UTSA-280 (the squarate linker is well restricted). Noted that, the squarate linker in UTSA-280 is rotation-forbidden.

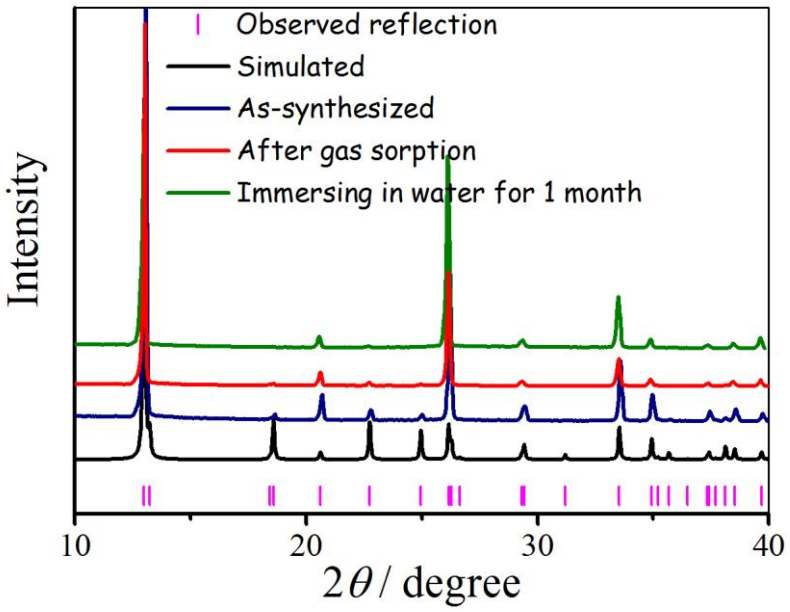

Supplementary Figure 3. PXRD patterns of different UTSA-280 samples.

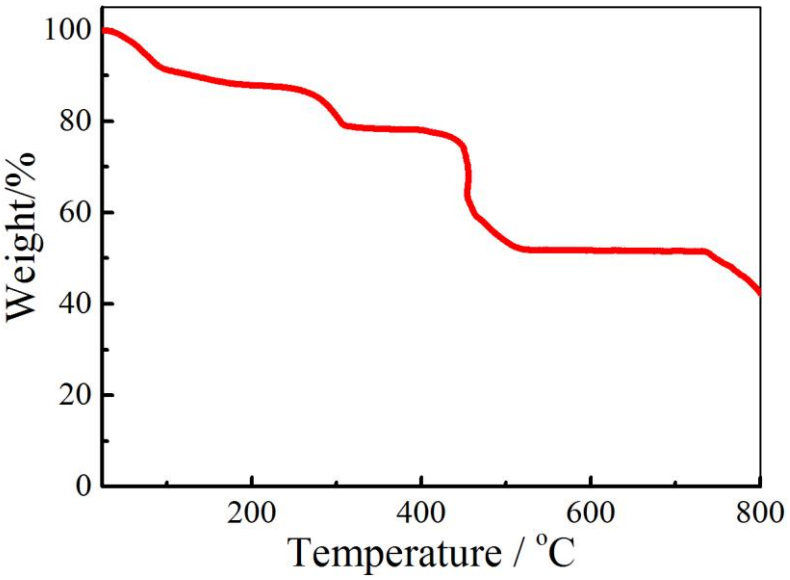

Supplementary Figure 4. TGA curve of **UTSA-280⊃H_2O**.

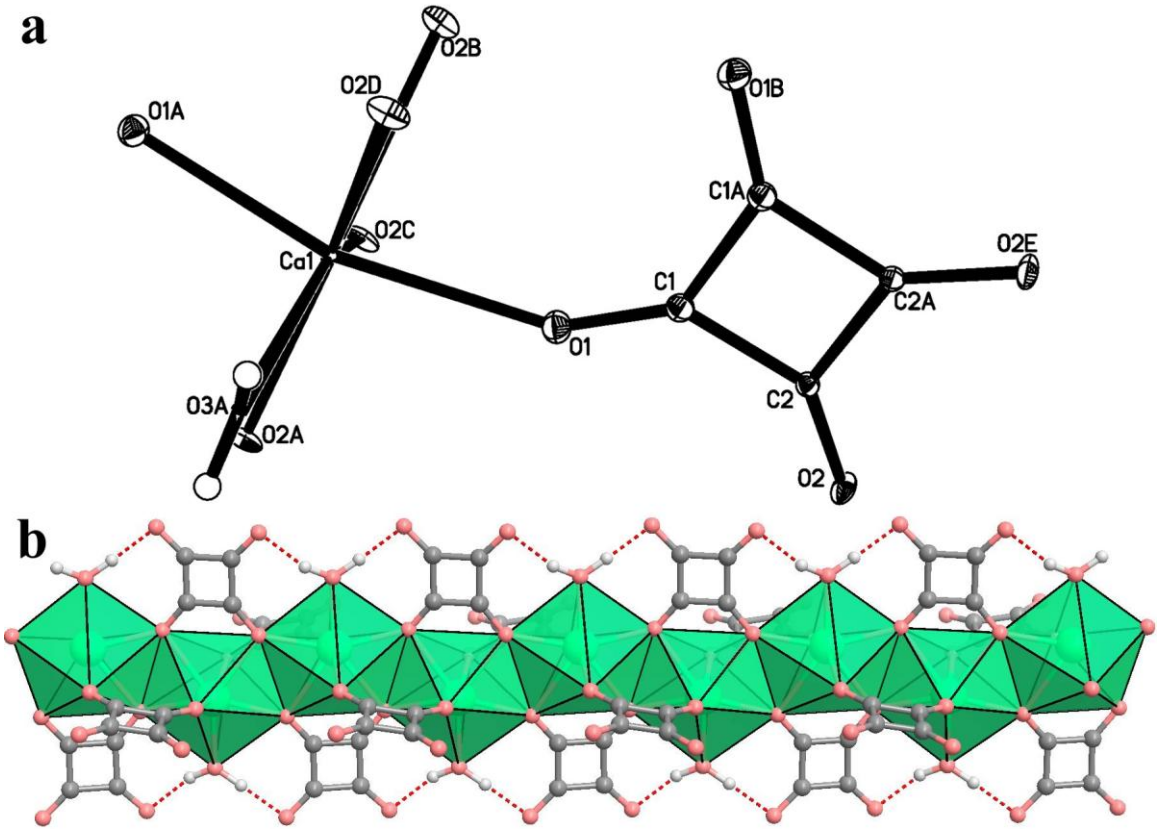

Supplementary Figure 5. (**a**) The coordination model in guest-free UTSA-280 shown as ellipsoids and (**b**) related one dimensional infinite calcium-oxo chain with hydrogen bonding. For coordinated water molecule, only one possibility position is presented in this work.

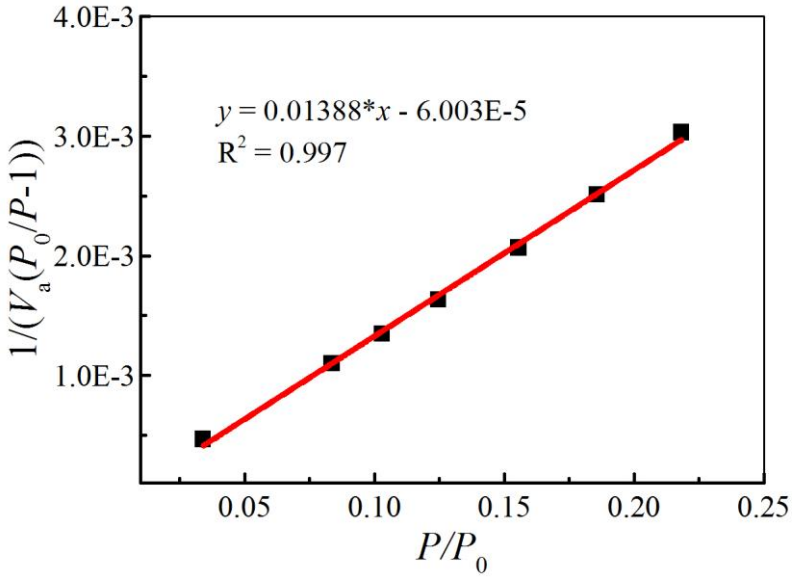

Supplementary Figure 6. Calculation of BET surface area for UTSA-280 based on CO_2 adsorption isotherm at 195 K.

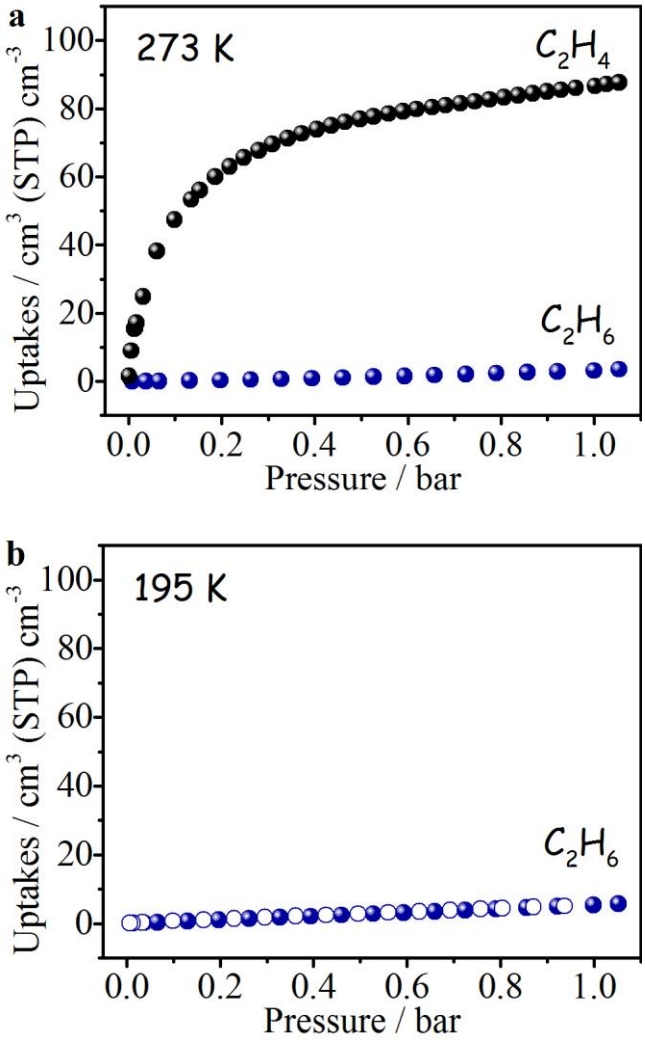

Supplementary Figure 7. Sorption isotherms of UTSA-280 for C_2H_4 and C_2H_6 at different temperatures.

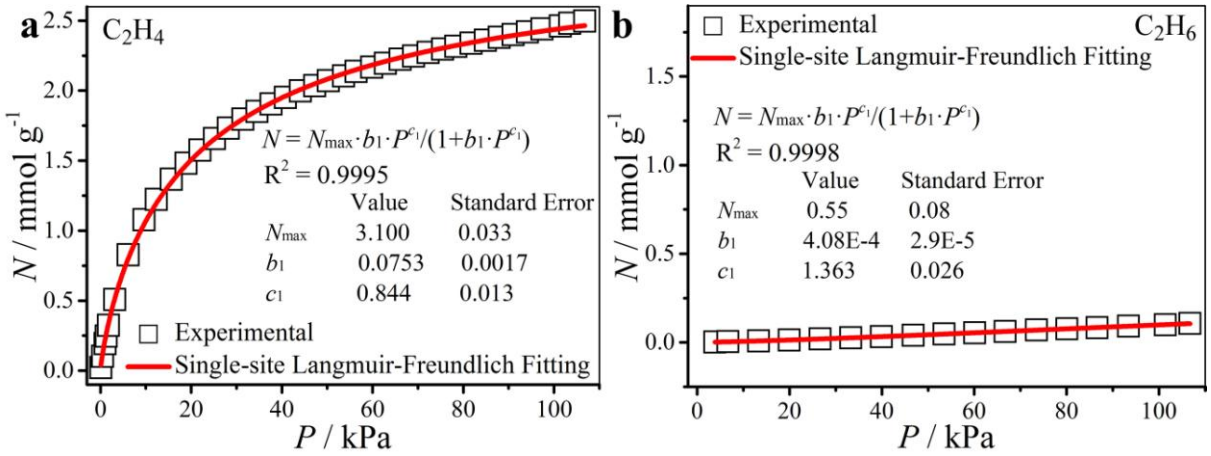

Supplementary Figure 8. Langmuir-Freundlich fitting of the C_2H_4 (**a**) and C_2H_6 (**b**) sorption data at 298 K for UTSA-280.

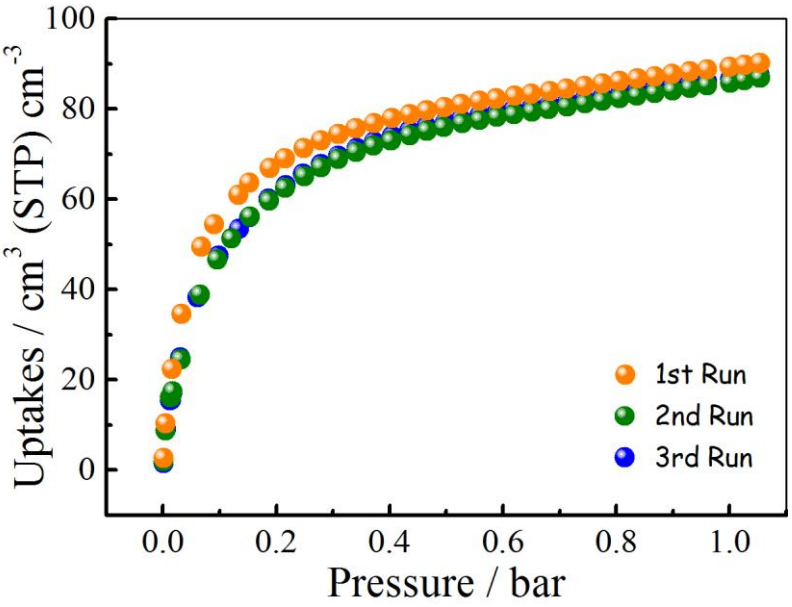

Supplementary Figure 9. Multiple cycles of C_2H_4 adsorption isotherms for **UTSA-280** at 273 K.

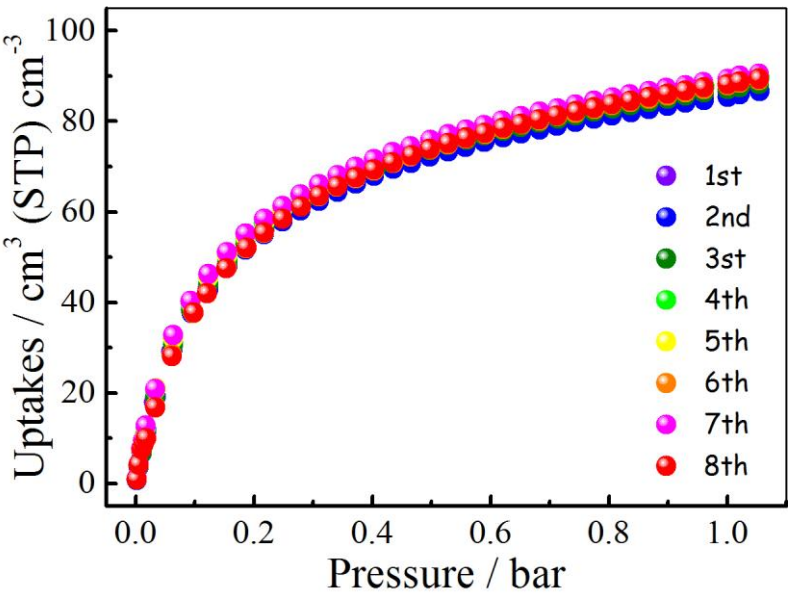

Supplementary Figure 10. Multiple cycles of C_2H_4 adsorption isotherms for **UTSA-280** at 298 K and 0–1 bar.

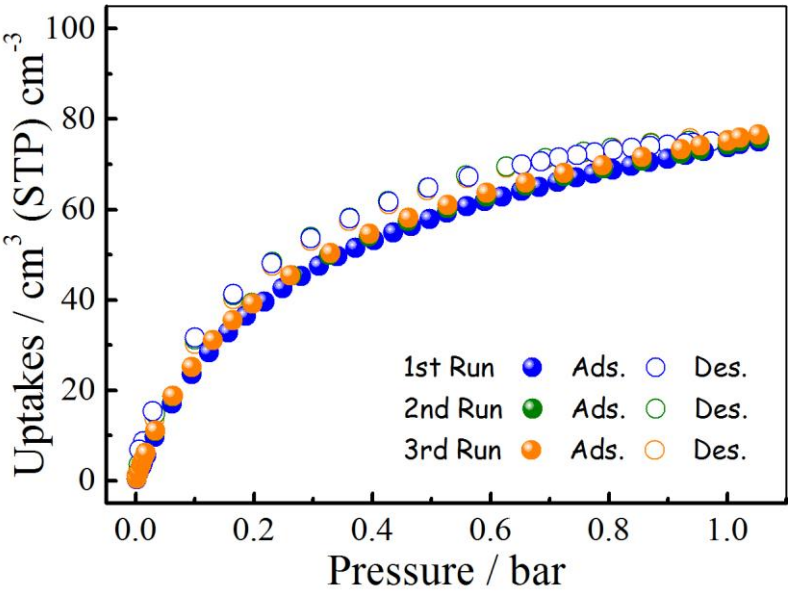

Supplementary Figure 11. Multiple cycles of C_2H_4 sorption isotherms for **UTSA-280** at 313 K.

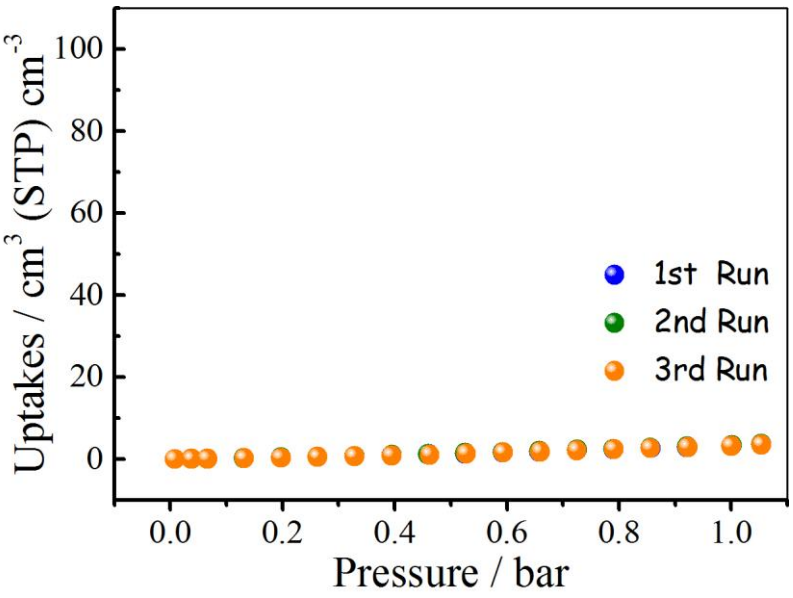

Supplementary Figure 12. Multiple cycles of C_2H_6 adsorption isotherms for **UTSA-280** at 273 K.

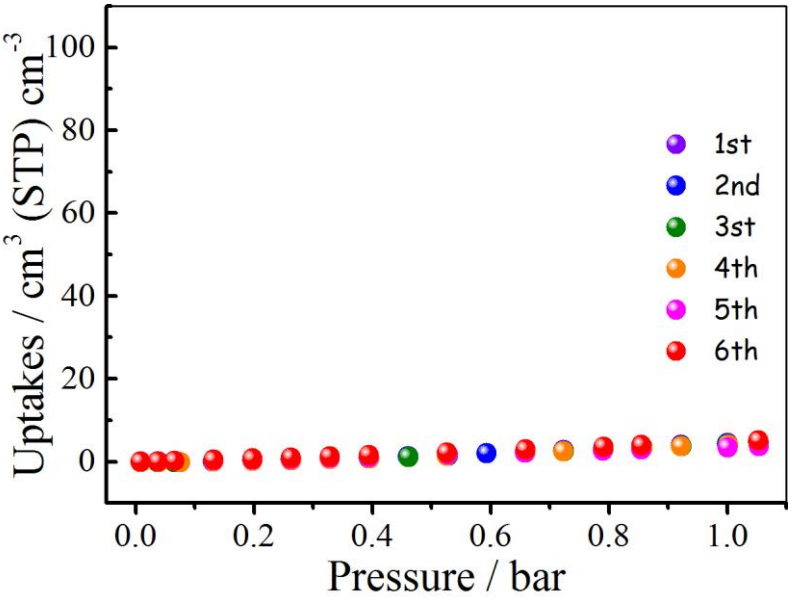

Supplementary Figure 13. Multiple cycles of C_2H_6 adsorption isotherms for **UTSA-280** at 298 K.

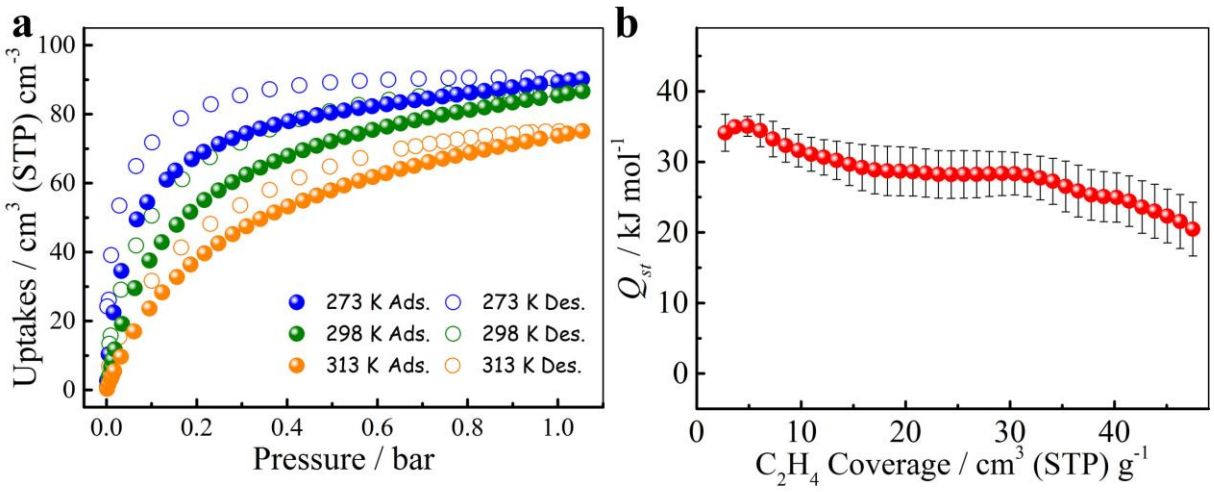

Supplementary Figure 14. (**a**) Sorption isotherms of UTSA-280 for C_2H_4 at different temperatures. (**b**) Isosteric heats of C_2H_4 adsorption (Q_{st}) calculated using the Clausius-Clapeyron equation, with error bars shown in black.

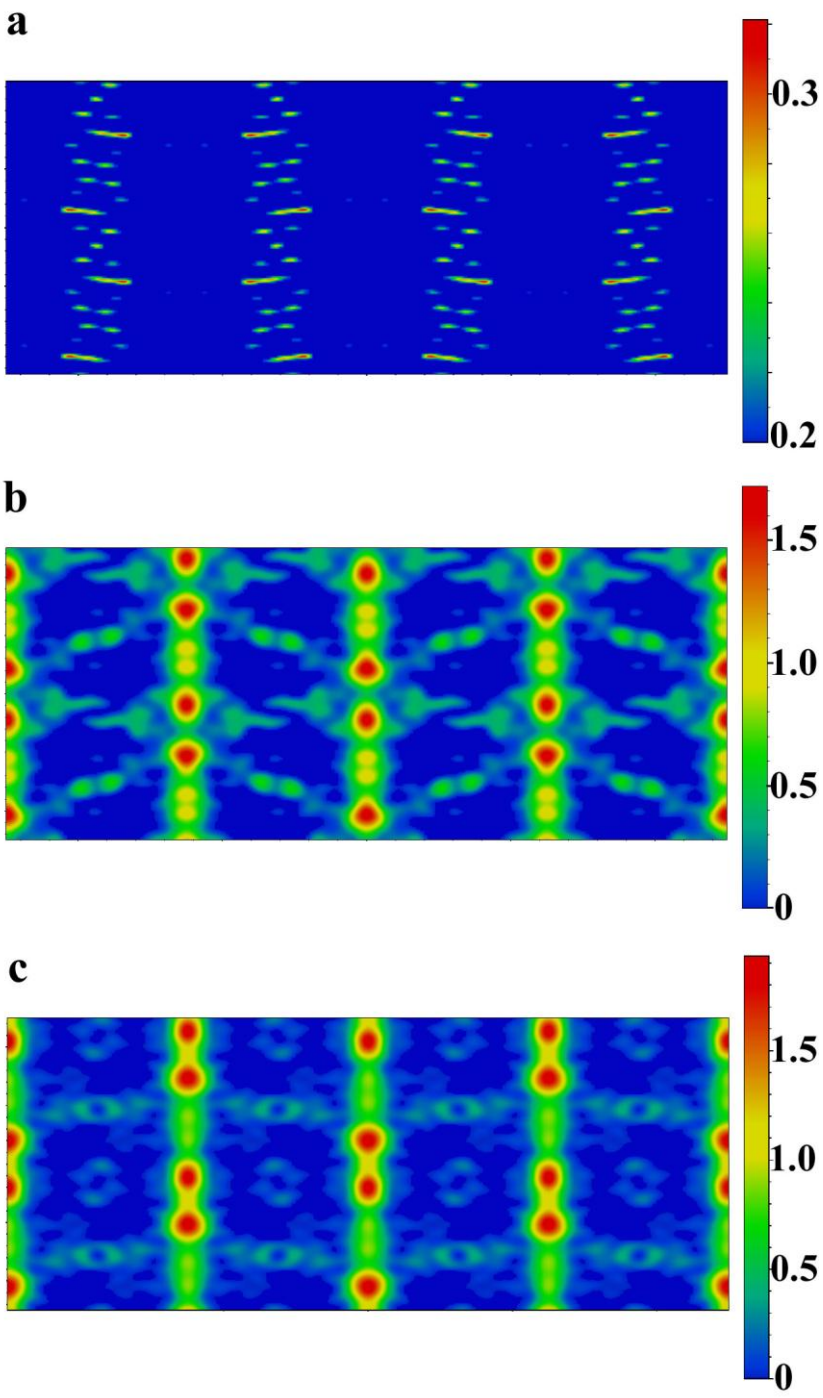

Supplementary Figure 15. Electron density maps of (**a**) UTSA-280, (**b**) UTSA-280·0.16C_2H_4 and (**c**) UTSA-280·0.20C_2H_4.

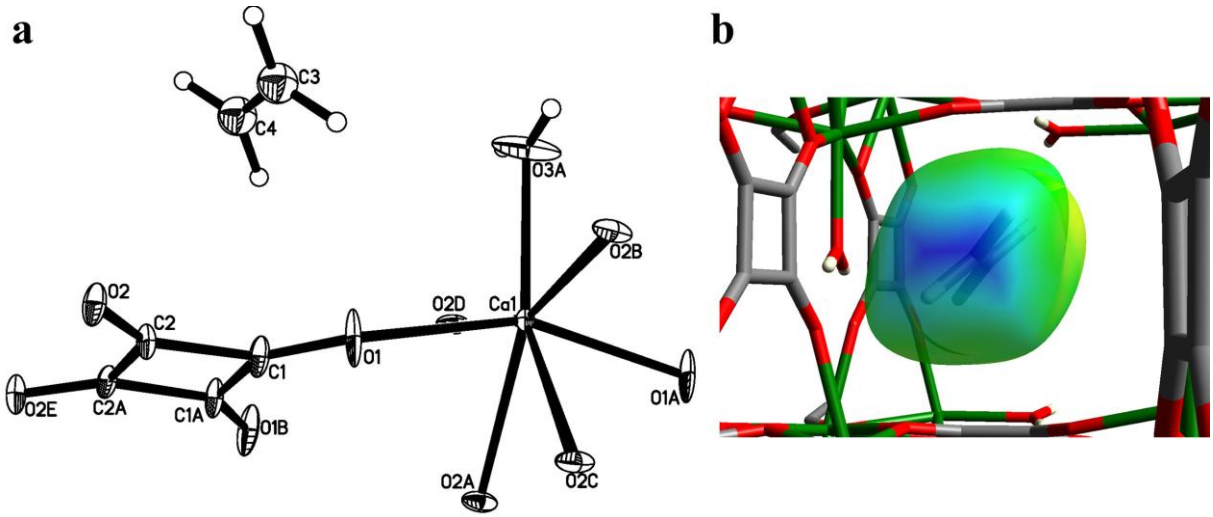

Supplementary Figure 16. Single-crystal X-ray structure of UTSA-280·0.20C_2H_4. (**a**) The coordination model shown as ellipsoids. (**b**) Hirshfeld surface (de) displaying weak host-guest interactions in UTSA-280.

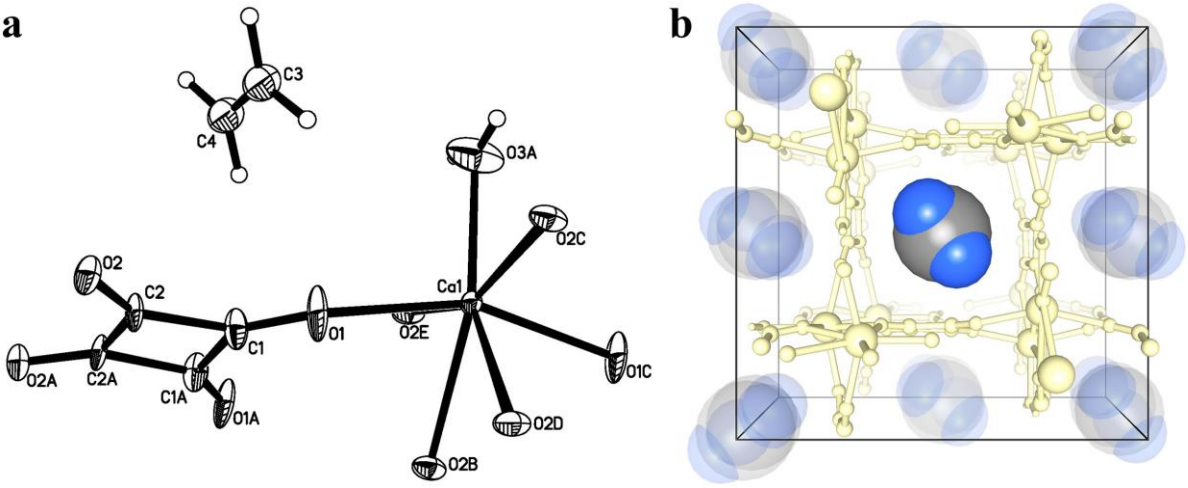

Supplementary Figure 17. Single-crystal X-ray structure of UTSA-280·0.16C_2H_4. (**a**) The coordination model shown as ellipsoids and (**b**) the corresponding cell unit.

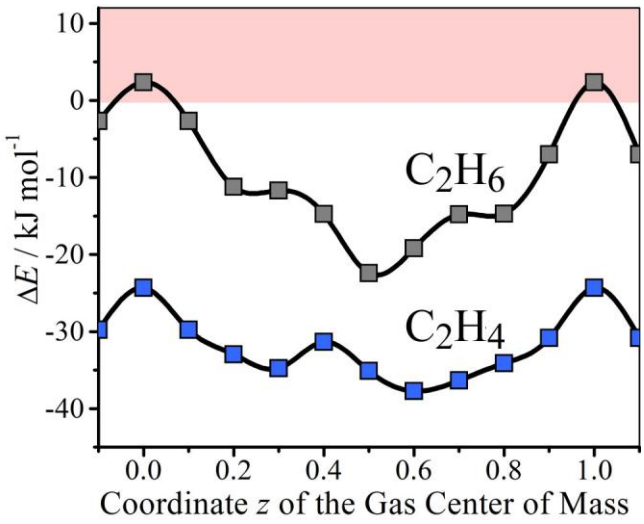

Supplementary Figure 18. The DFT-D calculated potential energy variation for C_2H_4/C_2H_6 molecule with hypothetical moving along the 1D pore channel of UTSA-280 (the coordinate *z* represents position along the crystallographic *c* axis). The static gas binding energy is shown as a function of the coordinate *z* of the molecule center of mass. Note that the C_2H_6 binding is overall much weaker than C_2H_4 binding in UTSA-280, and the energy value changes from negative to positive at *z*~0, suggesting the presence of a significant diffusion barrier for C_2H_6.

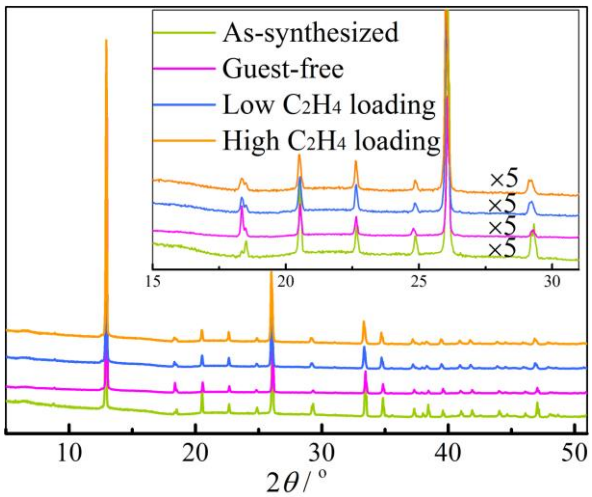

Supplementary Figure 19. Comparison of PXRD patterns for UTSA-280 under different conditions. There is no apparent shift in the positions of all peaks, indicating a high framework lattice rigidity of this MOF. Shown as inset is an enlarged view.

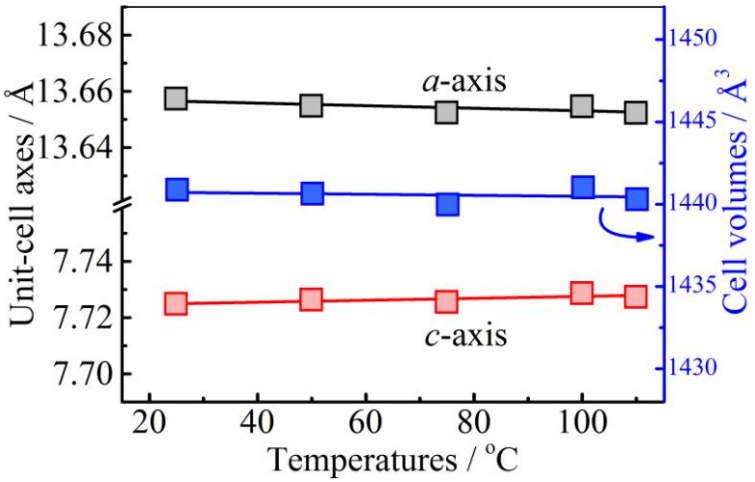

Supplementary Figure 20. Variable-temperature unit-cell parameters for UTSA-280, obtained from Pawley refinements of the corresponding PXRD patterns. The cell volume variation of this MOF, $\Delta V/V$ = 1 Å^3/1440.6 Å^3= 0.07%, which is less than that of rigid MOF-5 (0.8%, *Science 309, 1350-1354, 2005*). The corresponding linear thermal expansion coefficient is $<5\times10^{-6}$ K^{-1}, which is also less than those of typical rigid MOFs (MOF-5: -13×10^{-6} K^{-1}, *Angew. Chem. Int. Ed. 46, 4496-4499, 2007*; ZIF-8: 12×10^{-6} K^{-1}, *Chem. Commun. 54, 9651-9654, 2018*). The low thermal expansion of UTSA-280 supports the rigidity of framework, although indirectly.

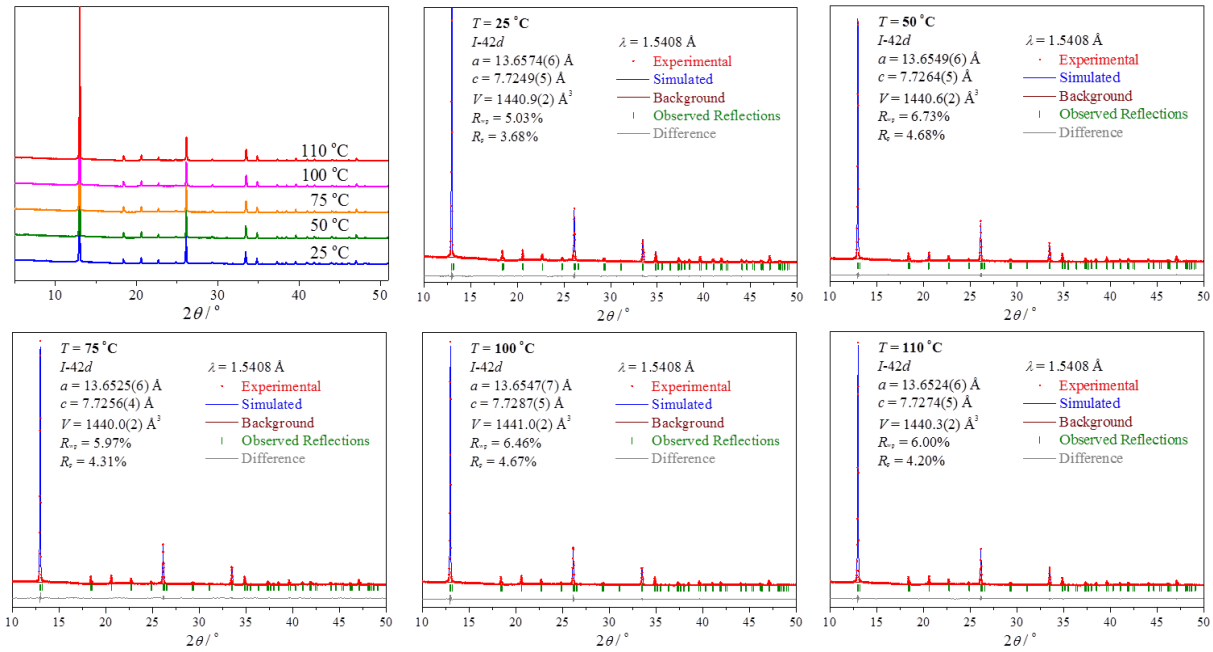

Supplementary Figure 21. Variable-temperature PXRD patterns for UTSA-280 and the corresponding Pawley refinements. Unit-cell parameters were obtained by Pawley refinements using the Reflex module of Materials Studio.

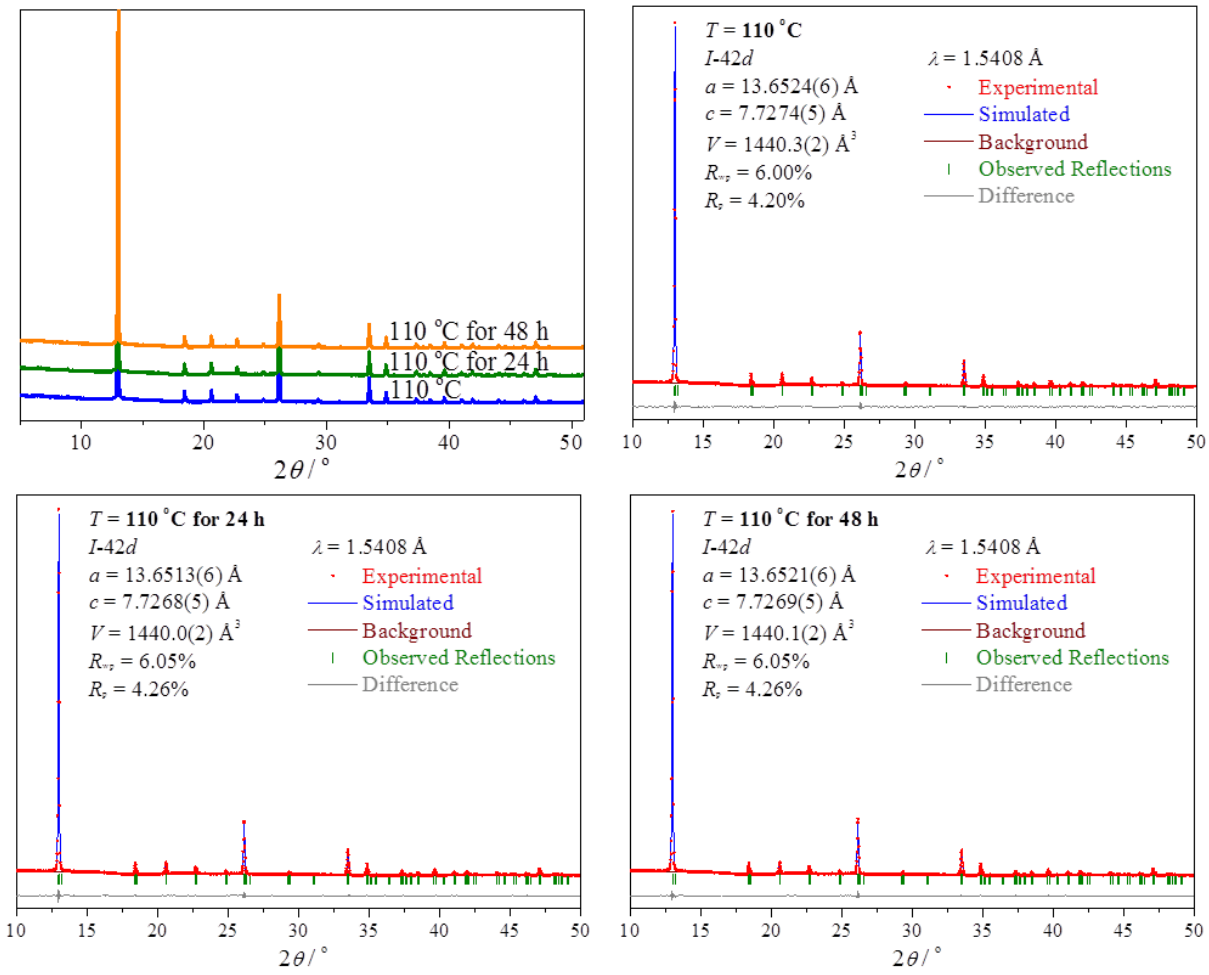

Supplementary Figure 22. PXRD patterns for UTSA-280 after cycling drying under 110 °C, and the corresponding Pawley refinements.

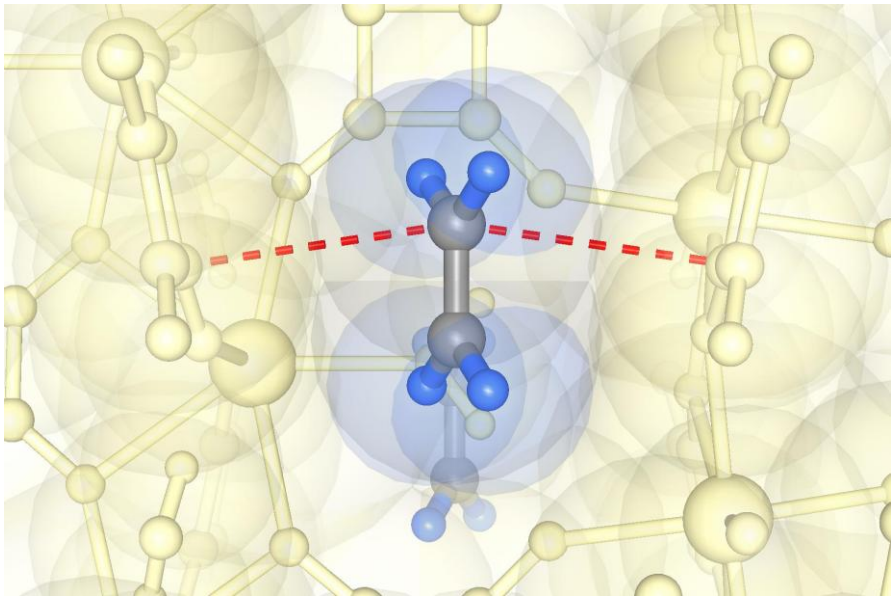

Supplementary Figure 23. Schematic picture showing the DFT optimized C_2H_4 configuration in UTSA-280⊃C_2H_4.

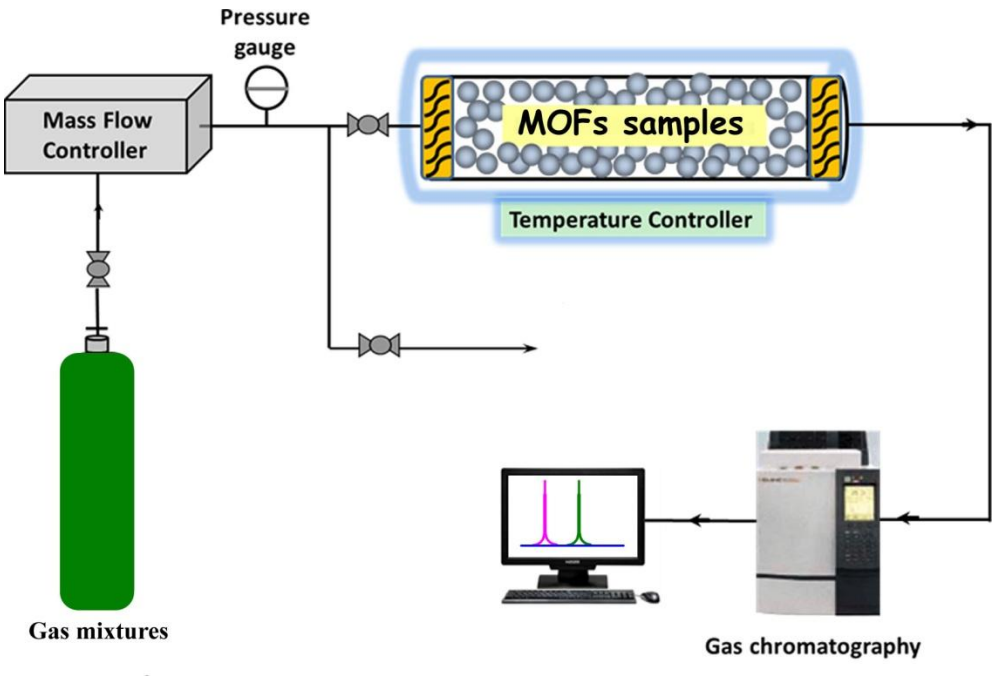

Supplementary Figure 24. Schematic illustration of the apparatus for the breakthrough experiments.

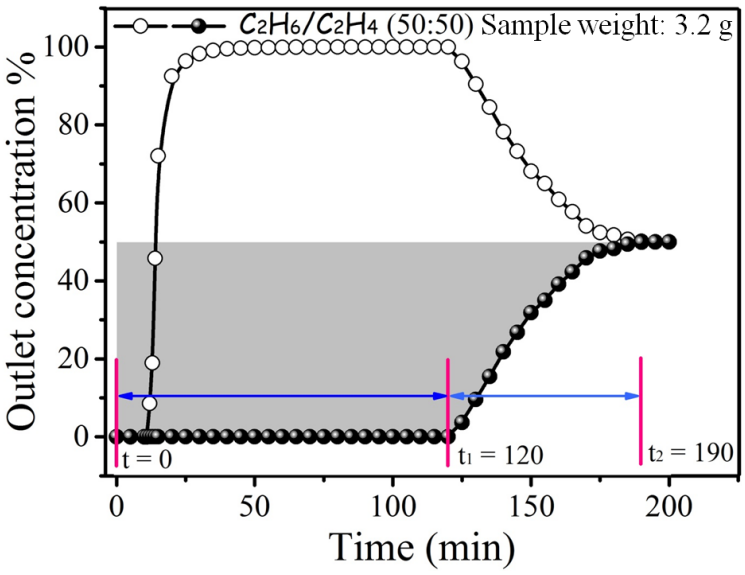

Flow rate of C_2H_4 (50%):
q = 1 mL/min = 0.0408 mmol/min

During the duration before breakthrough point 0–t_1:
The captured amount of C_2H_4:
$Q = qt_1$ = 0.0408 mmol/min × 120 min = 4.90 mmol, corresponding to 1.53 mmol/g.

The maximum loading for C_2H_4 during the time interval 0–t_2 :

$$Q_{max} = q\int_0^{\infty}[C_i^0 - C_i(t)]dt = 5.95 \text{ mmol}$$

corresponding to 1.86 mmol/g.

Supplementary Figure 25. The calculation for captured amount of C_2H_4 during the breakthrough process in UTSA-280. During the duration before the breakthrough point (0–t_1), the captured C_2H_4 is 4.90 mmol (110 cm^3), corresponding to 1.53 mmol/g. Considering the continuous C_2H_4 adsorption during the mass transfer zone (t_1–t_2), the integration of the grey area above the entire breakthrough curve gave the maximum loading of UTSA-280 to be 5.95 mmol (133 cm^3), corresponding to 1.86 mmol/g, which is about 90% of its theoretical capacity under the same pressure (2.05 mmol/g).

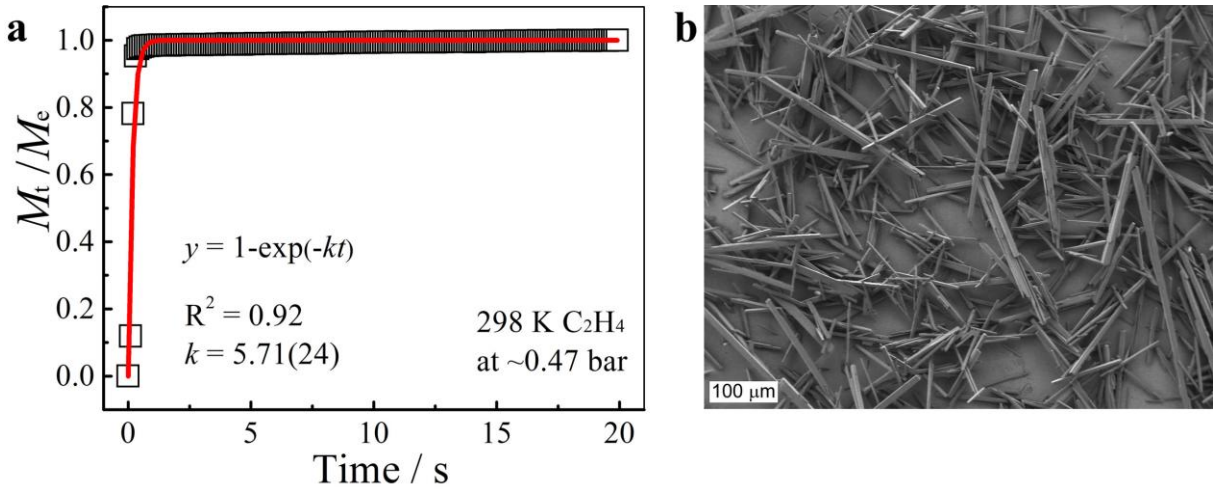

Supplementary Figure 26. (**a**) Kinetic profile of UTSA-280 for C_2H_4 adsorption at 298 K and equilibrium pressure of ~0.47 bar. (**b**) An SEM image of large-scale sample used to evaluate gas diffusivity (particle length on the channel direction are ca. 160 μm). Based on linear driving force model, the diffusion coefficient was estimated to 2.4 $\times 10^{-9}$ m^2/s, which is slightly lower than those of most MOFs (for C_2H_4 and similar gases, 10^{-9}–10^{-8} m^2/s, from *J. Phys. Chem. C 116, 23556−23568, 2012*). Field-emission scanning electron microscopy (SEM) measurement was performed on a JEOL JSM-7800F Prime scanning electron microscope.

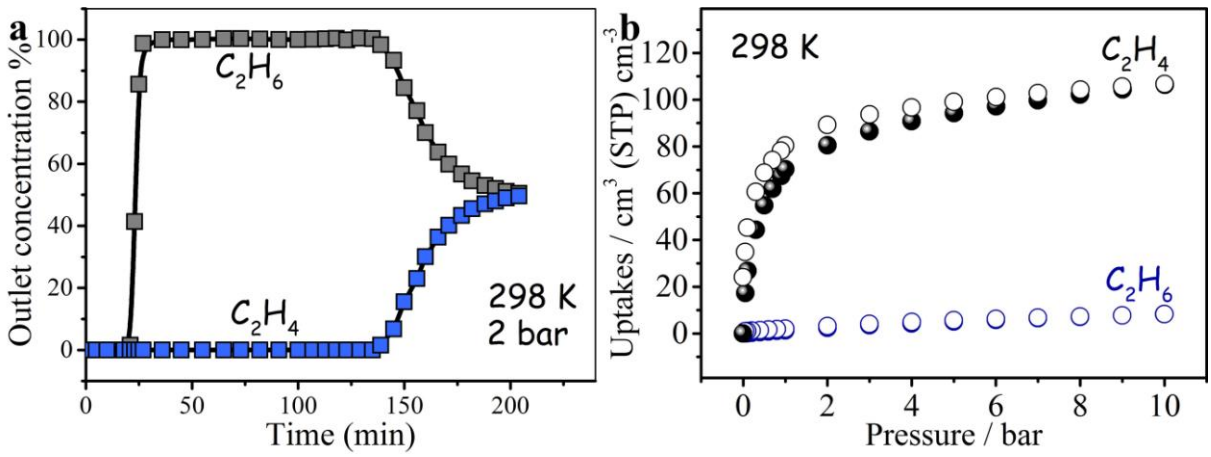

Supplementary Figure 27. (**a**) Breakthrough curves of UTSA-280 for equimolar binary mixture of C_2H_4/C_2H_6 at 298 K and 2 bar (flow rate: 2 mL/min). The integration of the area above the entire C_2H_4 breakthrough curve gave a maximum loading of 2.1 mol/kg for C_2H_4 enriched from equimolar C_2H_4/C_2H_6 mixture. (**b**) Sorption isotherms of UTSA-280 for C_2H_4 and C_2H_6 at 298 K, 10 bar. The large scale sample (3.1 g) was vacuumed for activation at ambient condition.

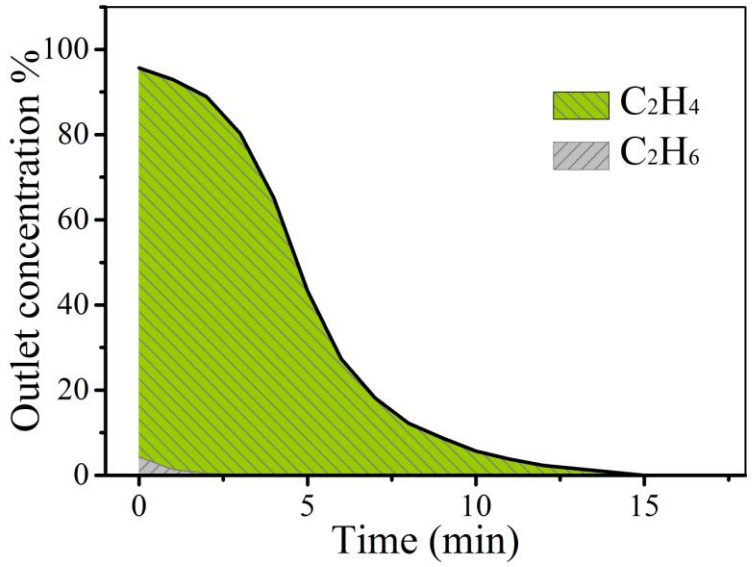

Supplementary Figure 28. Concentration curve of the desorbed C_2H_4 from UTSA-280 during the regeneration process of the fixed bed (saturated by 50/50 C_2H_4/C_2H_6 mixture). Desorption was carried out by applying vacuum at 298 K. Notably, starting from 50/50 C_2H_4/C_2H_6 mixture, the total purity of the enriched C_2H_4 is up to >99.2% after one single separation cycle.

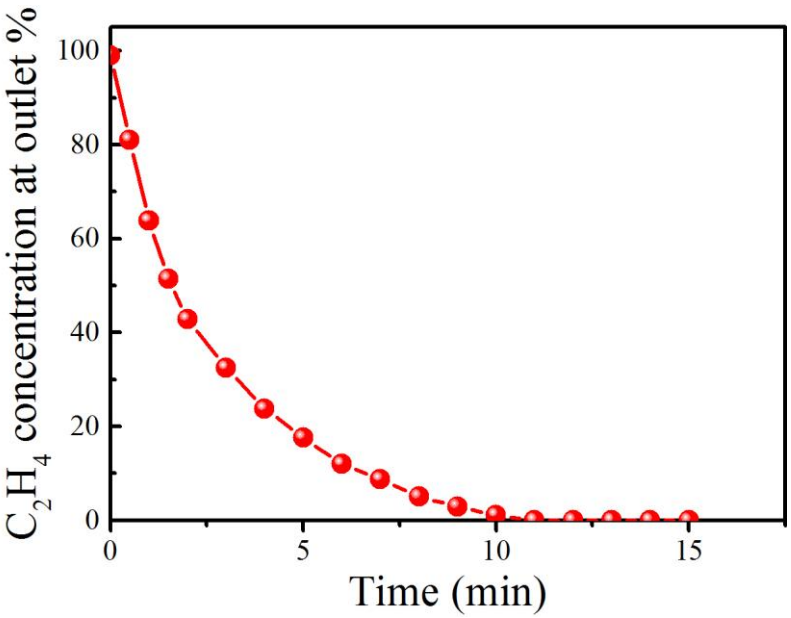

Supplementary Figure 29. Regeneration of UTSA-280 under a He flows at 353 K revealed that the adsorbed gas can be completely recovered within ten minutes. Concentration curve of the desorbed C_2H_4 from the fixed bed during the regeneration process of UTSA-280. Desorption was carried out by purging He (50 standard cubic centimeters per minute) at 353K. Notably, all the adsorbed ethylene can be completely removed from the column in approximately 10 minutes by a helium gas purge.

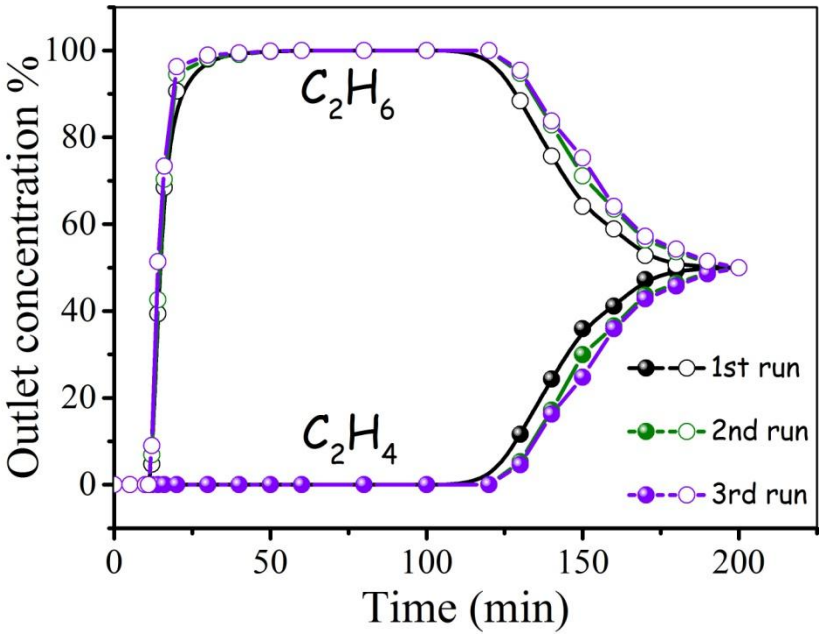

Supplementary Figure 30. Multiple cycles of breakthrough curves for equimolar binary mixture of C_2H_4/C_2H_6 at 298 K and 1 bar. The breakthrough experiments were carried out in a packed column at a flow rate of 2 standard cubic centimeters per minute. Points are experimental data, and lines are drawn to guide the eye.

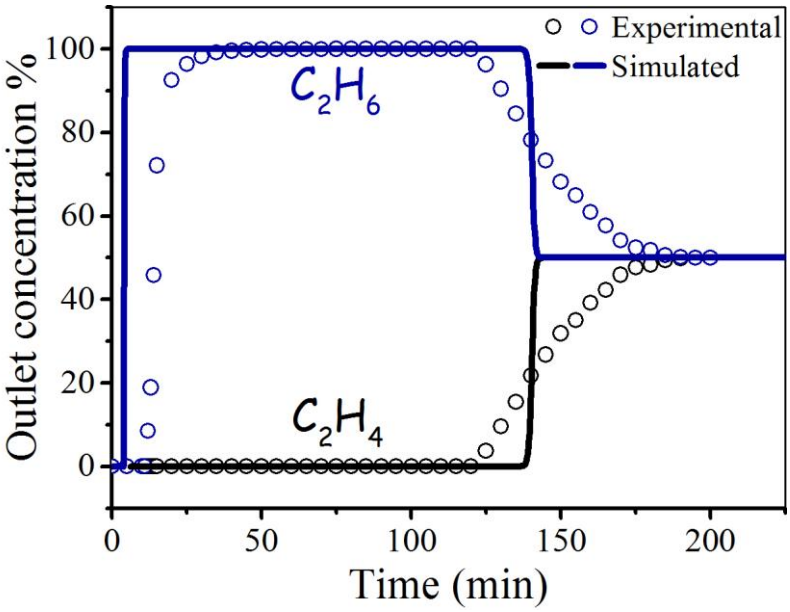

Supplementary Figure 31. Transient breakthrough of C_2H_4/C_2H_6 mixture (50/50, v/v) in an adsorber bed packed UTSA-280. The total bulk gas phase is at 298 K and 100 kPa. The partial pressures of C_2H_4, and C_2H_6 in the inlet feed gas mixture are, respectively, p_1 = 50 kPa, p_2 = 50 kPa. The simulated breakthroughs are somewhat sharper than those observed experimentally. That is because, in the simulation, intra-crystalline diffusional influences are ignored. The distended characteristics of the experimental breakthroughs with UTSA-280 are because of finite diffusional resistances.

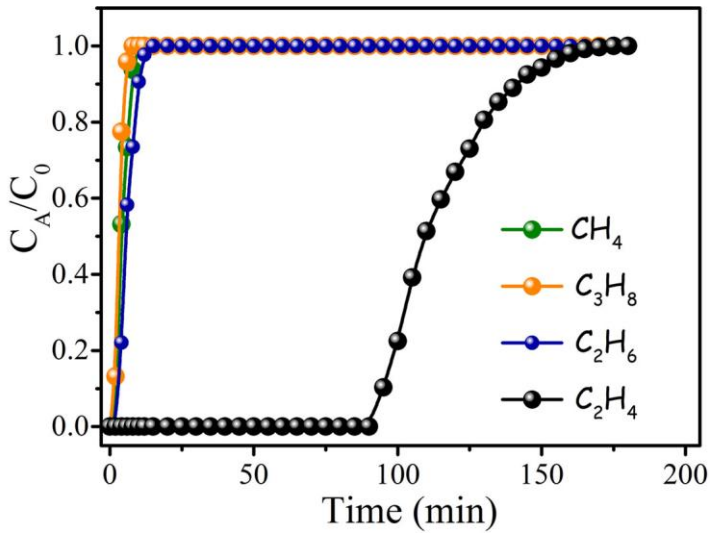

Supplementary Figure 32. Multi-component breakthrough curves for quaternary mixture of $CH_4/C_2H_4/C_2H_6/C_3H_8$ (45/25/25/5) at 298 K and 1 bar. The breakthrough experiments were carried out in a packed column at a flow rate of 2 standard cubic centimeters per minute. Points are experimental data, and lines are drawn to guide the eye.

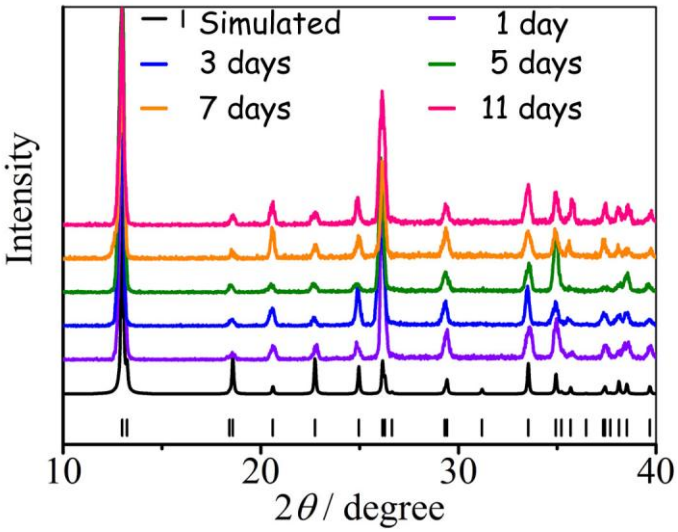

Supplementary Figure 33. Powder X-ray diffraction (PXRD) experiments showing the stability of UTSA-280 after immersing in water for various time.

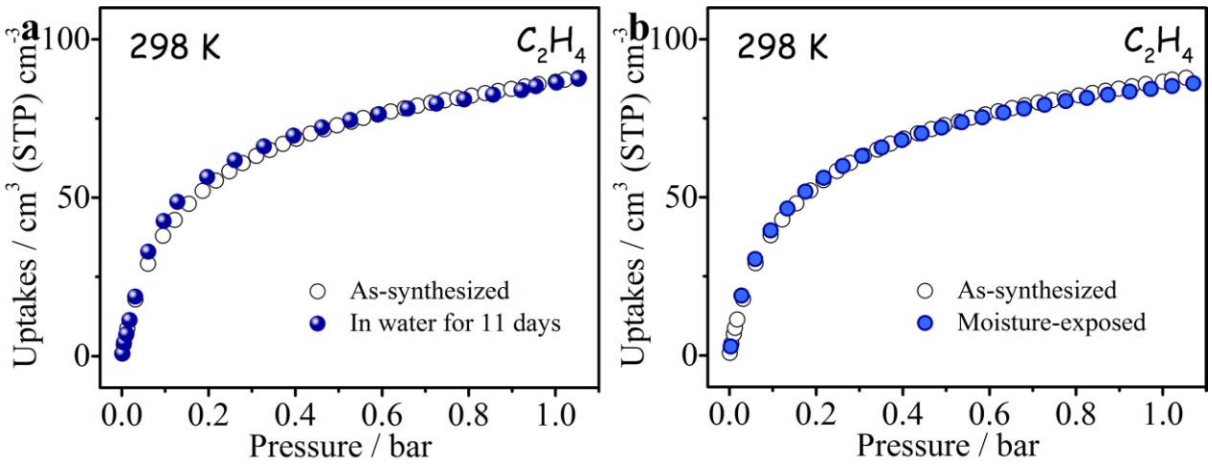

Supplementary Figure 34. The C_2H_4 adsorption isotherms for activated UTSA-280 at 298K, recorded before and after (**a**) immersing in water for 11 days or (**b**) air exposure for 3 day (humidity of 55%).

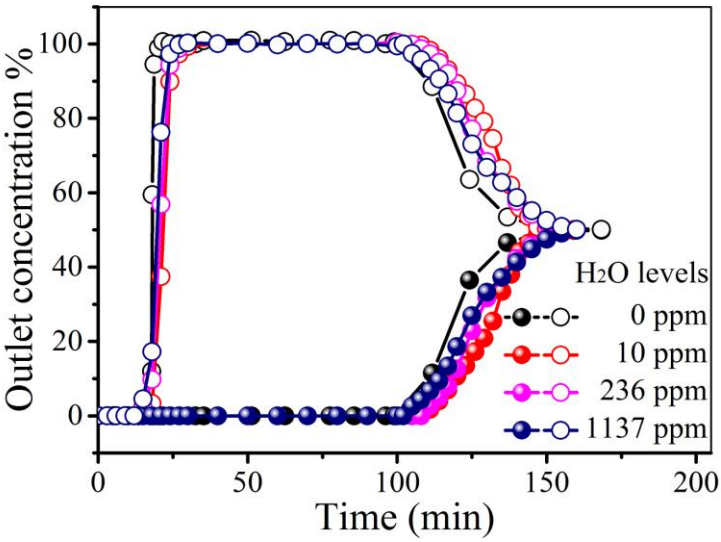

Supplementary Figure 35. Experimental column breakthrough curves for binary equimolar C_2H_4/C_2H_6 mixture with water of different levels, at 298 K and 1 bar. The breakthrough experiments were carried out in a packed column at a flow rate of 2 standard cubic centimeters per minute. Points are experimental data, and lines are drawn to guide the eye.

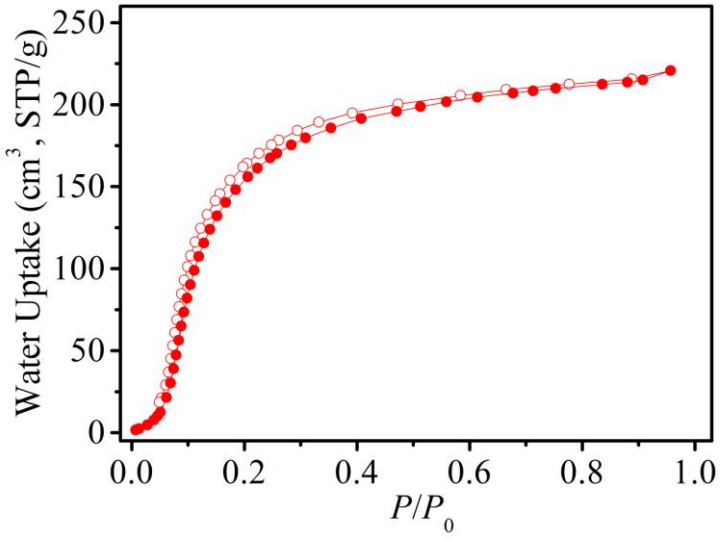

Supplementary Figure 36. Water sorption isotherms for UTSA-280 at 298 K.

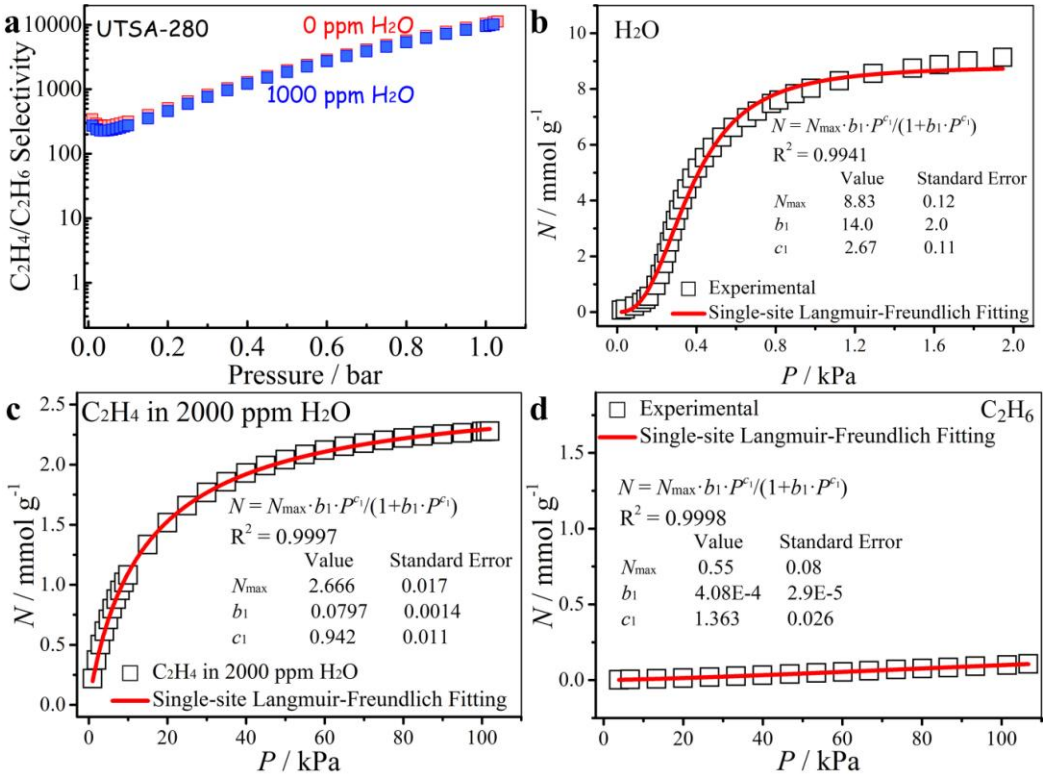

Supplementary Figure 37. (**a**) IAST adsorption selectivities of UTSA-280 for equimolar C_2H_4/C_2H_6 mixtures with different levels of H_2O at 298 K and (**b-d**) and the related Langmuir-Freundlich fittings.

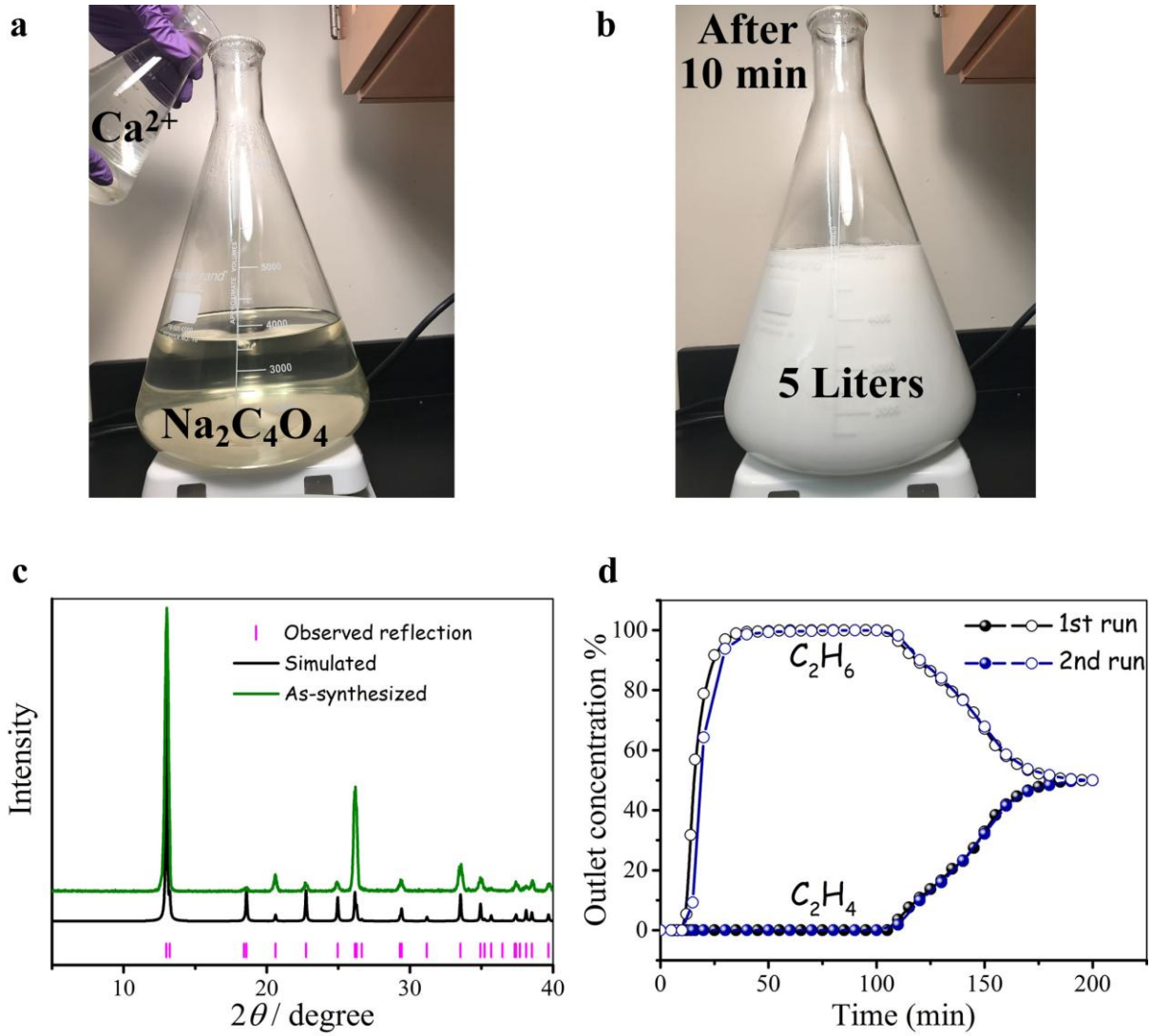

Supplementary Figure 38. Scale-up synthesis of UTSA-280. (**a**-**b**) About 0.22 kilogram UTSA-280⊃H_2O was quickly obtained by easily mixing a saturated aqueous solution of sodium squarate ($Na_2C_4O_4$) with an aqueous solution of $Ca(NO_3)_2 \cdot 4H_2O$. (**c**) The purity of the bulk products was confirmed by comparison of the simulated and experimental PXRD patterns. (**d**) Breakthrough curves of kilogram-scale UTSA-280 for equimolar binary mixture of C_2H_4/C_2H_6 at 298 K and 1 bar. The breakthrough experiments were carried out in a packed column at a flow rate of 2 standard cubic centimeters per minute.

Supplementary Table 1 to 4

Supplementary Table 1. Comparison of physical parameters of C_2H_4 and C_2H_6 [2].

	Molecular weight (g/mol)	Kinetic diameter (Å)	Boiling points (K)	Polarizability (10^{-25} cm^3)	Dipole moment (10^{-18} esu cm)	Quadruple moment (10^{-26} esu cm^2)
C_2H_4	28.05	4.163	169.4	42.5	0	1.5
C_2H_6	30.07	4.443	184.5	44.3–44.7	0	0.65

Supplementary Table 2. Crystal data and structure refinements of **UTSA-280** with different inclusions.

Complex	**UTSA-280**	**UTSA-280·0.20C_2H_4**	**UTSA-280·0.16C_2H_4**	**UTSA-280·H_2O**
Formula.	$C_4H_2CaO_5$	$C_{4.4}H_{2.8}CaO_5$	$C_{4.32}H_{2.64}CaO_5$	C_4CaO_6
F.W.	170.14	175.75	174.62	184.12
Temperature/K	200(2)	298(2)	298(2)	200(2)
Crystal system	Tetragonal	Tetragonal	Tetragonal	Tetragonal
Space group	*I*−42*d*	*I*−42*d*	*I*−42*d*	*I*−42*d*
a /Å	13.6557(2)	13.6335(7)	13.6152(1)	13.575(2)
c /Å	7.7174(3)	7.6869(18)	7.6790(1)	7.687(2)
volume/Å^3	1439.13(6)	1428.8(4)	1423.48(4)	1416.6(6)
Z	8	8	8	8
D_{calc}/g cm^{-3}	1.570	1.634	1.616	1.727
μ / mm^{-1}	7.327	7.401	7.425	7.615
*F*000	688	714	695	736
R_{int}	0.0448	0.0338	0.0567	0.0288
$R_1{}^a$ *I>2θ*	0.0649	0.0489	0.0747	0.0632
$wR_2{}^b$*I>2θ*	0.1696	0.1402	0.2029	0.1734
$R_1{}^a$ (all data)	0.0674	0.0512	0.0806	0.0632
$wR_2{}^b$ (all data)	0.1702	0.1424	0.2211	0.1734
GOF	1.104	1.067	1.135	1.225

$^aR_1 = \Sigma||F_o|-|F_c||/\Sigma|F_o|$, $^bR_{w2} = [\Sigma w(F_o^2-F_c^2)^2/\Sigma w(F_o^2)^2]^{1/2}$.

Supplementary Table 3. Langmuir-Freundlich parameter fits for C_2H_4 and C_2H_6 at 298 K in UTSA-280.

Adsorbates	N^{max} (mmol/g)	b (kPa^{-1})	1/n
C_2H_4	3.10	0.0753	0.84387
C_2H_6	0.55	4.0792E-4	1.3631

Supplementary Table 4. Summary of the adsorption uptakes, selectivities and heat of adsorption data for C_2H_4 and C_2H_6 in various ethylene sorbents.

	Surface area (m^2/g, BET)	Pore size (Å)	C_2H_4 uptake at 1.0 bar (mmol/g)	C_2H_6 uptake at 1.0 bar (mmol/g)	Temperature (K)	Selectivity for 50/50 C_2H_4/C_2H_6 mixture[a]	Q_{st} (C_2H_4, kJ/mol)[b]
HKUST-1 [3]	1500-2100	10, 14	7.20	6.03	303	3.6	39
NOTT-300 [4]	1370	6.5×6.5	4.28	0.85	293	48.7	16
FeMOF-74 [5]	1350	~12	6.28	5.10	318	13.6	47.5[c]
CoMOF-74 [6]	1341	~12	6.21	5.25	318	5.82	43.6[c]
Fe_2(*m*-dobdc) [7]	1295	~12	7.0	6.0	298	25	55
(Cr)-MIL-101-SO_3Ag [8,9]	1374	/	3.26	1.47	296	9.7	63
	1253	15, 18	4.32	1.22	303	16	120
PAF-1-SO_3Ag	783	~8.0	4.06	2.23	296	27	106
Zeolite 5A [10]	457-600	~5	2.45	1.72	303	4.5	37[c]
NaETS-10 [11]	289	~8	1.7	1.3	298	14	/
ITQ-55 [12]	/	2.07×5.86	1.28[d]	0.76[e]	303	90	/
UTSA-280	331	3.8×3.8	2.5	0.098	298	>10000[a]	34.1

[a] IAST selectivity, these values are only for the qualitative comparison purpose;
[b] Q_{st} values at low surface coverage;
[c] Highest Q_{st} values at different surface coverage.
[d] Measured at 0.45 bar.
[e] Measured at 0.6 bar.

Supplementary References

1 Webster, C. E., Drago, R. S. & Zerner, M. C. Molecular Dimensions for Adsorptives. *J. Am. Chem. Soc.* **120**, 5509-5516 (1998).

2 Li, J.-R., Kuppler, R. J. & Zhou, H.-C. Selective gas adsorption and separation in metal-organic frameworks. *Chem. Soc. Rev.* **38**, 1477-1504 (2009).

3 He, Y., Krishna, R. & Chen, B. Metal-organic frameworks with potential for energy-efficient adsorptive separation of light hydrocarbons. *Energy Environ. Sci.* **5**, 9107-9120 (2012).

4 Yang, S. *et al.* Supramolecular binding and separation of hydrocarbons within a functionalized porous metal–organic framework. *Nat. Chem.* **7**, 121-129 (2014).

5 Bloch, E. D. *et al.* Hydrocarbon Separations in a Metal-Organic Framework with Open Iron(II) Coordination Sites. *Science* **335**, 1606-1610 (2012).

6 Geier, S. J. *et al.* Selective adsorption of ethylene over ethane and propylene over propane in the metal-organic frameworks M_2(dobdc) (M = Mg, Mn, Fe, Co, Ni, Zn). *Chem. Sci.* **4**, 2054-2061 (2013).

7 Bachman, J. E., Kapelewski, M. T., Reed, D. A., Gonzalez, M. I. & Long, J. R. M_2(*m*-dobdc) (M = Mn, Fe, Co, Ni) Metal–Organic Frameworks as Highly Selective, High-Capacity Adsorbents for Olefin/Paraffin Separations. *J. Am. Chem. Soc.*, **139**, 15363-15370 (2017).

8 Chang, G. *et al.* Immobilization of Ag(i) into a metal-organic framework with -SO3H sites for highly selective olefin-paraffin separation at room temperature. *Chem. Commun.* **51**, 2859-2862 (2015).

9 Zhang, Y. *et al.* Highly selective adsorption of ethylene over ethane in a MOF featuring the combination of open metal site and [small pi]-complexation. *Chem. Commun.* **51**, 2714-2717 (2015).

10 Mofarahi, M. & Salehi, S. M. Pure and binary adsorption isotherms of ethylene and ethane on zeolite 5A. *Adsorption* **19**, 101-110 (2013).

11 Anson, A., Wang, Y., Lin, C. C. H., Kuznicki, T. M. & Kuznicki, S. M. Adsorption of ethane and ethylene on modified ETS-10. *Chem. Eng. Sci.* **63**, 4171-4175 (2008).

12 Bereciartua, P. J. *et al.* Control of zeolite framework flexibility and pore topology for separation of ethane and ethylene. *Science* **358**, 1068-1071 (2017).

Disclaimer: Certain commercial suppliers are identified in this paper to foster understanding. Such identification does not imply recommendation or endorsement by the National Institute of Standards and Technology, nor does it imply that the materials or equipment identified are necessarily the best available for the purpose.